UNIVERSITÀ DI PARMA

UNIVERSITA' DEGLI STUDI DI PARMA

DOTTORATO DI RICERCA IN
" *Scienze Mediche e Chirurgiche Traslazionali* "

CICLO XXXIV

Identification of an Epi-Metabolic Dependency on EHMT2/G9a in T-cell Acute Lymphoblastic Leukemia

Coordinatore:
Chiar.mo Prof. Nicola Sverzellati

Tutore:
Chiar.mo Prof. Giovanni Roti

Dottorando: Anna Montanaro

Anni Accademici 2018/2019 – 2021/2022

SUMMARY

ABSTRACT

Background: The identification of genes involved in DNA methylation and post-translational histone modifications in hematologic malignancies offers an opportunity for novel therapeutic intervention, geared towards reversing or modulating epigenetic events underpinning these diseases. In fact, in acute myeloid leukemia (AML) and myelodysplastic syndromes (MDS) methylation patterns are altered by mutations in *TET2*, *IDH1*, *IDH2*, *DNMT3A*, and *WT1* genes and matched therapies have demonstrated promising clinical activity. In T-cell acute lymphoblastic leukemia (T-ALL) the epigenetic driven approaches are not yet well validated, especially in the relapsed/refractory (R/R) setting. In this project, we sought to identify druggable epigenetic dependencies in T-ALL to anticipate potential synergistic interventions in R/R T-ALL.

Methods: We leveraged the results of a chemical and an epigenome-centered shRNA screen to identify chromatin modifier dependencies in T-ALL. We prioritized the conserved protein lysine H3K9me2-1 methyltransferase, G9a/EHMT2 based on the effect of targeted inhibition on cell viability and the preferential expression in leukemia vs. normal bone marrow. We described the phenotypic consequences of G9a loss due to small molecule inhibition or genetic suppression. The preponderance of results pointed to a role of G9a in the control of effectors of glycogen metabolism. We confirmed this as follows:1) functionally by glycolytic fluxes and mitochondrial dysfunction analysis, 2) transcriptionally by overlapping a geneset in which we suppressed G9a using small molecules or CRISPR/Cas9, with curated transcription factor GEO signatures to identify

common denominators of G9a signaling. Finally, we validated our hypothesis in 3D scaffolds and orthotopic xenograft T-ALL models.

Results: We identified *EHMT2* as a transcriptional dependency in T-ALL by the intersection of a shRNA and chemical screens both focused on epigenetic modifiers. Competitive and non-competitive G9a inhibitors, BIX01294, UNC0638 and UNC0642, or genetic G9a suppression decreases T-ALL proliferation drifting the cells into a late apoptotic stage. At the same conditions, the level of H3K9me2 selectively decreases compared to other epigenetic markers, suggesting the on-target effect of the observed phenotype. G9a deprived T-ALL cells present with an increased number of autophagic vacuoles containing glycogen. Interestingly glycogen accumulation is sustained by the inactivation of Glycogen Synthase Kinase 3 (*GSK-3*) in multiple G9a null T-ALL cell lines. We next asked whether G9a alters glucose metabolism and demonstrated a reduction of oxygen consumption upon G9a inhibitors treatment suggesting that G9a alters the balance between glycolysis and glycogenesis. Consistently the lack of glucose, secondary to 2-deoxy-d-glucose (2-DG) treatment rescues the formation of autophagosomes upon G9a treatment. Transcriptional enrichment analysis of *EHMT2* loss showed that the metabolic sensor *SESN2* is repressed upon G9a modulation, and in turn, loss of *SESN2* recapitulates the effect seen with G9a inhibition. Finally, we demonstrated that UNC0642 impairs leukemia growth both in 3D scaffold T-ALL from clinical samples and in a T-ALL xenograft orthotopic model where the loss of H3K9me2 parallels the antileukemia effect seen with this drug.

Summary/Conclusion: In conclusion, we identified G9a as an epigenetic vulnerability in T-ALL. Corollary to this, we described a role of G9a in the control of a metabolic circuitry with *SESN2* and *GSK-3* as downstream effectors of an autophagic cell death.

INTRODUCTION

Normal T-cell development is a strictly regulated, multistep process in which hematopoietic progenitor cells differentiate into functionally diverse T-lymphocyte subsets after their migration into the thymus microenvironment. The different checkpoints, covering thymic colonization, lineage commitment, and definitive differentiation,(1) are orchestrated by diverse transcriptional regulatory networks and transitions between epigenetic states in response to cytokine receptor activation. During this fine-tuned developmental process, inappropriate activation of T-cell acute lymphoblastic leukemia (T-ALL) oncogenes and loss of tumor suppressor gene activity will coordinately push thymic precursors into uncontrolled clonal expansion and cause T-ALL (2).

T-ALL is an aggressive hematologic disease that arises from the malignant transformation of T-cell progenitors and represents the 15% of pediatric and 25% of adult ALL cases. Unfortunately, about 20% of T-ALL patients often relapse during treatment resulting in a 5-year survival rate of relapsed T-ALL. The current strategies of treatment of T-ALL are characterized with high dose of multiagent chemotherapy and is highly effective in most childhood leukemia patients, with overall survival rates reaching 85% in most pediatric protocols. Nevertheless, these aggressive treatment regimens are often associated with severe acute toxicities and long-term side effects. Despite the introduction of hematopoietic stem cell transplantations for refractory leukemias, the clinical outcome of these high-risk, primary resistant tumors remains extremely poor (3).

More than a decade ago, using karyotyping, fluorescence in situ hybridization (FISH), array comparative genomic hybridization (arrayCGH) and microarray gene expression profiling, it has been possible classified the T-ALLs in well-defined genetic subgroups (4-6). Indeed, T-ALL can be divided into molecular-genetic subtypes characterized by unique gene expression signatures that relate to stages of T-cell differentiation at which the leukemic cells arrest. Each molecular-genetic subgroup shows characteristic genetic abnormalities that cause aberrant activation of specific T-ALL transcription factor oncogenes, including *LYL1*, *HOXA*, *TLX1*, *TLX3*, *NKX2-1*, *NKX2-2*, and *TAL1/LMO2* (7).

The introduction of targeted and next-generation sequencing techniques further broadened the genetic landscape of T-ALL, underlying genetic lesions that target genes with important roles in NOTCH1 signaling, cell cycle, hematopoiesis, signal transduction and ribosomal machinery. Some of them are aberrant expression of the *MEF2C* gene (8); genetic alterations in hematopoietic transcription factors such as *RUNX1*, *GATA3*, *BCL11B*, *PU.1*, and *ETV6* (9); activating mutations in critical mediators of cytokine receptor and Ras signaling, including *NRAS*, *KRAS*, *FLT3*, *IL7R*, *JAK1*, *JAK3*, *SH2B3*, and *BRAF*. Importantly, like in any other tumor entity, recent sequencing efforts revealed the implication of several key regulators of epigenetic modifiers such as *EZH2*, *EED*, *SUZ12*, *MLL2*, *BMI1*, *SETD2*, and *EP300* (10).

Epigenetic deregulation represents a core component of the molecular circuitry that is perturbed during T-cell transformation. Nevertheless, the molecular mechanisms that drive malignant T-cell development downstream of these epigenetic alterations remain

poorly understood and face us with the great challenge of translating this complex epigenetic information into the clinic as molecularly tailored epigenetic therapies.

It has been known since the early 1980s that also epigenetic abnormalities contribute to tumorigenesis by perturbing gene expression, not associated with alterations of the DNA sequences coding for the deregulated genes in question (11). There are several underlying mechanisms for switching genes on and off, including changes in DNA methylation, post-translational histone modifications, and altered expression patterns of long non-coding RNAs (lncRNAs) as regulatory elements in the epigenetic machinery to add another level of complexity to the epigenome (12).

However, detailed mechanistic analyses of epigenetic have long been hindered by a lack of effective technologies. With the use of modern next generation sequencing techniques for single cell and bulk analysis it is now possible to comprehensively investigate transcriptional and epigenetic heterogeneity and define their disease relevance. This is critically important for designing therapeutic targeting of epigenetic modifiers and novel biomarkers that measure their effect and predict responses.

Crucially, sequence-based deep learning methods can predict the impact of rare or never-seen variants that may be discovered with more sequencing, providing information that cannot be readily learned from phenotypic association studies of large genomic databases (13). In combination with genome editing tools such as CRISPR–Cas9 to control various cis elements and trans factors, single-cell epigenomics assays could be

applied to test the causality of chromatin modifications and cellular heterogeneity in various systems. Moving forward, these techniques promise to provide detailed profiles of cellular states and will facilitate a much deeper understanding of the underlying mechanisms that control gene expression heterogeneity (14).

Given the rapidly expanding repertoire of epigenetic players implicated in cancer and more specifically in T-ALL, the emerging opportunities to therapeutically target the tumor epigenome suggests that disruption of the epigenetic balance can drive cellular transformation.

In a recent landmark study, Huether et al. (15) sequenced 633 epigenetic regulatory genes in over 1000 pediatric tumors representing 21 different cancer subtypes and found T-ALL to be among the tumors with the highest frequency of mutations in regulators that code for factors involved in epigenetic regulation, such as recurrent genomic lesions in a variety of genes involved in DNA methylation and post-translational histone modifications (PTMs) in T-ALL. This identification offers an opportunity for novel therapeutic intervention, geared towards reversing or modulating epigenetic events underpinning the leukemic state.

Central to epigenetics is the diverse repertoire of covalent modifications made to histone proteins and nucleic acids that cooperatively regulate chromatin structure and gene expression (16). Epigenetic modifications are reversible and dynamically regulated, initially attached and subsequently removed by specialized chromatin-modifying enzymes

known as epigenetic ‘writers’ and ‘erasers’, respectively (17). In addition to covalent modifications made to histones and nucleic acids, epigenetic regulation encompasses dynamic spatio-temporal positioning of nucleosomes (known as chromatin remodelling), regulation of the three-dimensional conformation of chromatin and nuclear topology, the localization and activity of RNA binding proteins and RNA splicing machinery as well as transcribed elements of the non-protein coding genome such as long non-coding RNAs and enhancer RNAs (18).

Besides the core replicative histones (that is, H2A, H2B, H3 and H4), histone variants also exist and are assembled into nucleosomes in a replication independent manner. Some of the better studied histone lysine methylations occur predominantly on histones H3 and H4, including histone H3 lysine 4 (H3K4), lysine 9 (H3K9), lysine 27 (H3K27), lysine 36 (H3K36), lysine 79 (H3K79) and histone H4 lysine 20 (H4K20). Each of these lysines can exist in four methyl states (unmodified, monomethylated (Kme1), demethylated (Kme2) and trimethylated lysine (Kme3)); alternatively, they can exist in acetylated or other acylated forms yielding staggering complexity, although the abundance and relative weight of various PTMs in terms of function can vary (19).
These chromatin variations establish a fundamental means of regulating essentially all the DNA- templated processes such as gene transcription, DNA replication, DNA damage repair and DNA recombination.

Histone PTMs and DNA methylation, established and removed by antagonizing enzymes of writers and erasers, respectively, regulate chromatin- based processes both in cis and

in trans. In cis, histone PTMs change structural or physical properties of nucleosomes, for example, increasing DNA accessibility or neutralizing the negative charge of DNA via histone charge- altering modifications (for example, acetylation and phosphorylation).
In trans, chromatin modification serves as a context- dependent docking site for recruiting readers or other effectors (20). It is worth noting that a good number of writers and erasers also harbor a chromatin reader module, thereby opening various possibilities for potential crosstalk among chromatin modifiers including self-propagation, cooperation, competition, or antagonism.

From a therapeutic perspective, small-molecule inhibitors of reader domains are a promising strategy for targeting lysine methylation signaling pathways. Overall, given the number of proteins that are regulated by lysine methylation and the complexity associated with sensing and transducing these molecular events, there is tremendous untapped potential in selectively targeting components of this network to treat human disease. Recently, several molecules have entered early clinical phase testing in hematologic neoplasms. Tazemetostat, the histone methyltransferase inhibitor (HMT) inhibitor of enhancer of zeste homologue 2 (EZH2) (21), is currently in a single agent open-label, phase 1/2 trial in patients with B-cell lymphomas and in combination with prednisolone in diffuse large B-cell lymphoma (DLBCL) (NCT01897571). Pinometostat (EPZ-5676), an inhibitor of the disruptor of telomeric silencing-1 gene (*DOT1L*), has been assessed in phase 1 dose-escalation studies in pediatric and adult patients with relapsed and refractory AML and ALL (22, 23). Similarly, pharmacologic inhibition of menin-lysine methyltransferase 2A (*KMT2A*) binding proved to be an effective antileukemic strategy in

preclinical models of *KMT2A* related leukemias (24) and supported clinical trials evaluating menin inhibitors as targeted therapies in acute leukemia (25).

The G9a/GLP complex represents an additional, druggable methyl transferase target. In fact, several groups have developed inhibitors targeting G9a and GLP with high specificity (26-29). G9a and GLP are conserved protein lysine methyltransferases that contain a Su(Var), enhancer of zeste, trithorax (SET) domain. G9a localizes in euchromatin regions and regulates gene expression and chromosome structure through de novo mono- and di- methylation of histone H3 lysine 9 (H3K9me1/2). Di- and trimethylation of lysine 9 of histone H3 (H3K9) in gene promoters have been associated with transcriptional repression in several disease models (30, 31). *EHMT2*, which encodes for the G9a protein, has emerged as a potential tumor biomarker of aggressive cancers (31, 32).

In this work, the intersection of multiple “omics” approaches identified G9a as a therapeutic target in T-cell acute lymphoblastic leukemia (T-ALL), an aggressive neoplastic disorder of lymphoblasts committed to the T-cell lineage in need of new treatment modalities, particularly in relapsed/refractory cases (33). We determined that G9a suppression inhibits the metabolic sensor sestrin2 (*SESN2*), promotes lysosomal biogenesis and autophagic degradation and, ultimately leading to the inactivation of Glycogen Synthase Kinase 3 (GSK-3) and impaired glycogen metabolism.

MATERIALS AND METHODS

Cell Culture

Human cell lines SUPT1, MOLT16, LOUCY, DND41, HPB-ALL, and MOLT4 were purchased respectively from Leibniz-Institut DSMZ-German collection of microorganisms and cell cultures (Germany) and American Type Culture Collection (ATCC, Manassas, VA, USA); identities of ALL/SIL, KOPTK1, PF382, and SUPT11, were confirmed by PCR sequencing for known *NOTCH1* mutations and short tandem repeat (STR) loci profiling. CCRF-CEM, DU528, HSB2 and PEER were a gift from the Bradner lab (Dana-Farber Cancer Institute, Boston, MA, USA). HS-5 cells were a gift from Giuliani lab (University of Parma. Cells were cultured in RPMI 1640 or DMEM (Thermo Fisher Scientific, Waltham MA, USA, Waltham MA, USA #MT10040CV) with 10% fetal bovine serum (FBS) (Sigma-Aldrich, St. Louis, MO, USA, #F2442-500ML) and 1% penicillin-streptomycin (Thermo Fisher Scientific, Waltham MA, USA, #3MT30002CI) and incubated at 37°C with 5% CO_2.

Primary T-ALL Samples, T-lymphocytes, and murine Thymic cells

Primary patient leukemic cells or tissue biopsies were obtained under an approved protocol at the Parma University Hospital (n.18249/18/05/2017, n.265/2019) and according to the declaration of Helsinki guidelines for the protection of human rights. PB and BM samples were collected at the time of diagnosis. Mononuclear cells were isolated by density gradient centrifugation using LSM-lymphocyte separation medium (Cappel™ MP Biomedicals, LLC, Ohio, USA #50494). Lymphocytes were isolated from PBMC by using a CliniMACS Prodigy (Miltenyi Biotec, Bergisch Gladbach, Germany) and cultured for a short time using the same growth conditions described above. Cells were seeded in

384-well plates (Corning Life Sciences Plastic, Bedford MA, USA, #3570) at the final concentration of $0.02x10^6$/mL per condition. Small molecules were added with a nanometric dispenser Tecan D300e (Tecan Trading AG, Switzerland). Clinical samples were plated alive (trypan blue exclusion assay > 90% in all cases) and viability was assessed after 72 hours of drug treatment using a CellTiter-Glo ATP assay (Promega Corporation, Madison, WI, USA, #G7573). The analysis was performed using GraphPad Prism software (La Jolla, CA, USA) to calculate the IC_{50} and the areas under the curve (AUC) of drugs.

Murine thymic cells were isolated by enzymatic digestion (CorningTM RPMI-1640 with 1,5 µg/mL Collagenase/Dispase®, Roche, and 1 µl/ml Dnase I, ThermoFisher) 37 °C for 15 minutes. The supernatant fraction was collected in a 50 mL tube containing 10 mL of cold albumin-rich buffer (1X PBS [Ca2+/Mg2+-free] with 0,5 % Bovine serum albumin and 2mM ethylenediaminetetraacetic acid [EDTA]) to neutralize the enzymes. The operations were repeated 2 more times, until complete tissue digestion; then the pooled supernatants were centrifuged at 400 x g, 4 °C for 8 minutes. The pelleted cells were resuspended in 10 mL cold albumin-rich buffer and counted using a hemocytometer. The separation of the $CD25^-$ cells was performed using the mouse CD25 MicroBead Kit (MACS Milteny Biotec) according to manufacturer's instructions. Briefly, 2×10^8 cells were resuspended in 1,96 mL of albumin-rich buffer, added with 40 µL of CD25-PE-conjugated antibody and incubated for 10 minutes at 4°C. After washing, the cells were centrifuged and resuspended in 1,8 mL of albumin-rich buffer before the addition of 200 µL of anti-PE MicroBeads, followed by 15 minutes of incubation at 4°C. After being further washed

and centrifuged, pelleted cells were resuspended in 1 mL albumin-rich buffer. The cell suspension was applied onto a MS Column, previously assembled with a pre-separation filter and placed on the magnetic separator. The flow-through containing $CD25^-$ cells was collected in a 15 mL tube. Then, the column was removed from the magnetic separator to flush out and collect the $CD25^+$ cells in a separated tube for validation experiments.

Cell Viability, Proliferation and Apoptosis

ATP-based cell viability was determined using the CellTiter-Glo Luminescent Cell Viability Assay (Promega Corporation, Madison, WI, USA #G7573). Luminescence was measured using a Fluostar Omega instrument (BMG-labtech, Ortenberg, Germany) or a Victor X4 (Perkin Elmer, Waltham, MA, USA). Apoptosis was measured by Annexin V and propidium iodide (PI) staining using flowcytometry (Affymetrix, eBioscience, San Diego, CA, USA, 88-8007-74). Cells were analyzed by flow cytometry with a FACScan flow cytometer (BD, Franklin Lakes, NJ, USA or Beckman Culture-Cytomics FC 500, Life Sciences Division, Indianapolis, USA) and FlowJo V10 (Tree Star LLC, Ashland, OR, USA) analytical software.

Compounds were obtained from the following sources: BIX01294 (R&D Systems Inc., Minneapolis, MN, USA #3364/10mg, or Selleckchem, Houston, TX USA, #S8006/10mg); UNC0638 and UNC0642 were donated from Jian Jin (Icahn School of Medicine, Mt. Sinai, New York, NY) or purchased UNC0638 (Cayman Chemical, Ann Arbor, Michigan USA #1255580-76-7 or Selleckchem, #S8071); UNC0642 (Sigma-Aldrich, St. Louis, MO, USA, #SML1037 5 mg); compound E (ENZO Life Sciences, Farmingdale, NY, USA, #ALX-270-415-M001), vincristine sulfate (Tocris Bio-techne, Bristol, UK #1257); nelarabine (Tocris

Bio-techne, Bristol, UK # 6359); daunorubicin (Selleckchem, Houston, TX USA, #S3035); GSK126 (Selleckchem, Houston, TX USA, #S7061); SGC0946 (Selleckchem, Houston, TX USA, #S7079), C646 (Cayman Chemical, Ann Arbor, Michigan, USA, #10549); CTPB (Sigma Aldrich-Merck division Darmstadt, Germany #EP001); Bafilomycin A1 (InvivoGen, San Diego, CA, USA CAS88899-55-2), SB216763 (Selleckchem, Houston, TX USA, #S1075), CHIR 99021 (Selleckchem, Houston, TX USA, #S1263).

sgRNA Design

CRISPR sgRNA were designed using the Broad Institute guide designer which implements the Rule Set 1 sgRNA scoring algorithm. Guides were specifically designed to target the enzymatic domain (SET) of *EHMT2*. The complete DNA sequence of Human *EHMT2* was analyzed using the NCBI gene ID database. Below are the guide sequences.

EHMT2 sgRNA	End	Oligonucleotide Sequence	Target
#2	5’	CACCGGTGCAGCATGAAGACCCGGA	C-terminus SET domain
#2	3’	AAACTCCGGGTCTTCATGCTGCACC	C-terminus SET domain
#5	5’	CACCGTGGTTACACTCGAAAATCAG	Pre-SET domain
#5	3’	AAACCTGATTTTCGAGTGTAACCAC	Pre-SET domain

#6	5’	CACCGTTCGACTTAGACAACAAGG A	Interaction SET-H3
#6	3’	AAACTCCTTGTTGTCTAAGTCGAA C	Interaction SET-H3

Plasmids, Cloning and Lenti-viral constructs

Desalted oligonucleotides were synthesized by the Molecular Biology Core Facility (at Dana-Farber Cancer Institute, Boston, MA, USA). *EHMT2* target guide sequence cloning was done using the Lentiviral CRISPR tool box in the Genome-Scale CRISPR knockout protocol. CRISPR plasmids were digested using the FastDigest Esp11 (#FD0454), FastDigest Buffer (Thermo Fisher Scientific, Waltham MA, USA #B64) and Fast Alkaline Phosphatase (Life Technologies, Carlsbad, CA, USA, #EF0651). Digested plasmids were purified using the QIAquick Gel Extraction Kit (Qiagen, Hildberg, Germany, #28704). Oligos were annealed using T4 ligation buffer ((Fisher Scientific (Thermo Fisher Scientific), Waltham MA, #46300-018) and T4 PNK enzyme (supplemented with ATP), (New England Biolabs, Ipswich MA, USA, #M0201S). Transformation was done by heat-shock using One Shot Stbl3 Chemically Competent E. coli protocol (Life Technologies, Carlsbad, CA, USA, #C737303). Plasmid isolation was performed using the HiSpeed Plasmid Maxi Kit Qiagen (Qiagen, Hildberg, Germany, #12663).

SESN2 PLKO.1 based shRNA vectors were obtained from MERK (Sigma-Aldrich, St. Louis, MO, #SHCLNG-NM-031459) and sequences are listed below.

Catalog #	Oligos	shRNA number

TRCN0000142035	CCGGGCCCGAATCCTAGTTCAGTTTCTCGA GAAACTGAACTAGGATTCGGGCTTTTTTG	#1
TRCN0000143630	CCGGGAAGACCCTACTTTCGGATATCTCGA GATATCCGAAAGTAGGGTCTTCTTTTTTG	#2

Virus Production and Transduction of T-ALL Cell Lines

pCMV-VSV-G envelope vector and Delta 8.9 packaging plasmid constructs were used for making virus (Addgene, Cambridge MA, USA). 293T adherent were plated at 1.5 million/ml in DMEM media (Life Technologies, Carlsbad, CA, USA, # 11965118), 10% fetal bovine serum (FBS) (Sigma-Aldrich, St. Louis, MO, USA, #F2442-500ML) and 1% penicillin-streptomycin (Fisher Scientific (Thermo Fisher Scientific)), Waltham MA, #3MT30002CI) and incubated at 37°C with 5% CO_2, until confluent. DMEM media was aspirated from and replaced with 5 ml of RPMI media (with 10% FBS, 1% Penicillin Streptomycin). The transduction mix containing the entry and envelope vectors (VSVG/ Delta 8.9, CRISPR/Cas9 and sgRNA or shRNA constructs, FuGENE 6 Transfection Reagent (Promega Corporation, Madison WI, USA, #E2691) and Opti-MEM Reduced-Serum medium (1X) liquid (Life Technologies, Carlsbad, CA, USA, #31985062) was added to 293T cells. Virus mix was incubated at 37°C for 72 hours. Same day transduction of PF382 and SUPT1 cells was performed with non-frozen, freshly harvested virus as follows: 4 million cells were plated in 100 µl of RPMI media with polybrene in triplicate replicates in a round bottom 96 well plate and infected with 100 µl of virus. A double spin-infection was done at 2500 RPM for 2 hours at temperature of 25°C. Cells

were expanded at 24- and 48-hours post infection and selected in puromycin (1µg/ml) (Invitrogen, San Diego, CA, USA #ANT-PR-1) at the 72-hour time point.

Protein Sample Preparation

Whole cell protein lysate was extracted using 1X Cell Lysis buffer (Cell Signaling Technology, Danvers, MA, USA, #9803S) with Phospho-stop, Phosphatase Inhibitor (Sigma-Aldrich, St. Louis, MO, USA, #04906837001) or Protease/phosphatase Inhibitor Cocktail 100X (Cell Signaling Technology, Danvers, MA, USA, #58725) and Complete Mini, EDTA-free Protease Inhibitor (Sigma-Aldrich, St. Louis, MO, USA, #11836170001). Cytoplasmic and nuclear extractions were performed as described in the Nuclear Extract Kit (Active Motif, Carlsbad, CA, USA, #40010). The Abcam Histone Extraction Protocol was used for all histone extractions (Abcam, Cambridge, United Kingdom, #AB221031), with minor amendments. Cells were harvested and washed twice with ice-cold Phosphate Buffered Saline (PBS), then suspended in Triton Extraction Buffer (TEB: PBS containing 0.5% Triton X 100 (v/v), 2 mM phenylmethylsulfonyl fluoride (PMSF), 0.02% (w/v) NaN3). Cells were lysed on ice for 10 minutes with gentle stirring and centrifuged at 2000 RPM for 10 minutes at 4°C to spin down the nuclei. The supernatant was discarded. Nuclei were washed in half the volume of TEB and centrifugation repeated as before. The pellet was then re-suspended in 0.2 Na HCl and left overnight at 4°C. Samples were centrifuged at 6,500 XG for 10 minutes at 4°C to pellet debris. Supernatant containing the histone protein was collected for analysis by western blot.

Antibodies

Knockout of *EHMT2* was confirmed by western blotting of whole cell lysate using anti-G9a/EHMT2 (C6H3) rabbit monoclonal antibody (Cell Signaling Technology, Danvers, MA, USA, #3306S). Anti-GAPDH mouse monoclonal antibody (Santa Cruz Biotechnology, Dallas, TX, USA, #sc-47724) was used a loading control. For histone fractions the following antibodies were used: mouse monoclonal to histone H3 (di methyl K9) (Abcam, Cambridge, United Kingdom, #AB1220); rabbit polyclonal antibody to histone H3 (mono methyl K9) (Abcam, Cambridge, United Kingdom, #AB8896), rabbit polyclonal antibody to histone H3 (tri methyl K9) (Abcam, Cambridge, United Kingdom, #AB8898) . Anti-Histone 3 rabbit polyclonal antibody (total) was used as a loading control (Abcam, Cambridge, United Kingdom, #AB1791) and vinculin (Santa Cruz Biotechnology, Dallas, TX, USA, #sc-25336) was used as loading control for Whole cell lysate.

To assess the effect of G9a inhibitors on glycogen synthesis at the protein level, western blotting of whole cell lysate was performed using the following GSK-3 antibodies listed below: rabbit monoclonal antibody phosho-GSK-3α (Ser21) (#36E9), rabbit monoclonal antibody phospho-GSK-3β (Ser9, #9336S), rabbit monoclonal antibody total GSK-3α/β (D75D3) (#5676S), rabbit polyclonal phospho-mTOR(Ser2448)(#2971), rabbit polyclonal phospho-p70 S6 Kinase(Thr389)(#9205) (Cell Signaling Technology, Danvers, MA, USA).

To confirm *EHMT2*/G9a expression at a protein level in T-ALL cell lines with different *NOTCH1* status, western blotting was performed using G9a/EHMT2 (C6H3) rabbit monoclonal antibody (Cell Signaling Technology, Danvers, MA, USA, #3306S), EHMT1/GLP mouse monoclonal antibody (Abcam, Cambridge, United Kingdom, #AB41969) and Cleaved Notch1 (Val1744) (D3B8) rabbit monoclonal antibody (Cell

Signaling Technology, Danvers, MA, USA, #4147). Anti-GAPDH mouse monoclonal antibody (Santa Cruz Biotechnology, Dallas, TX, USA, #sc-47724).

Apoptosis and autophagy were assessed with the following antibodies: rabbit monoclonal antibody cleaved-PARP (#BK9541S), rabbit polyclonal antibody LC3B (#2775), sestrin2 (D1B6) rabbit monoclonal antibody (#8487) (Cell Signaling Technology, Danvers, MA, USA). HSP90 (4F10) mouse monoclonal antibody (Santa Cruz Biotechnology, Dallas, TX, USA, #sc-69703) and β-Actin (13E5) rabbit monoclonal antibody (Cell Signaling Technology, Danvers, MA, USA, #4970) were used as a loading control.

For chemiluminescence based development the following secondary antibodies were used: anti-mouse IgG, peroxidase-linked species-specific F (ab')2 fragment Fisher Scientific (Thermo Fisher Scientific, Waltham MA #45000680); anti-rabbit IgG, peroxidase-linked species-specific F(ab)2 fragment (from donkey), (Thermo Fisher Scientific, Waltham MA #45000680, MA #45000683). All fluorescent secondary antibodies used were obtained from LI-COR Biosciences, Lincoln, NE, USA. They include: IRDye 680LT Goat anti-Mouse IgG 0,1mg (#925-68020); IRDye 800CW goat anti-rabbit IgG 0,1mg (#925-32211); IRDye 680RD goat anti-rabbit IgG 0,1 mg (#925-68071).

Western Blotting

Proteins were quantified using Bio-Rad Protein Assay Dye Reagent (Bio-Rad Laboratories, Hercules, CA, USA, #5000006). For western blot immuno-detection, we used the Renaissance Western Blot Chemiluminescence reagent with enhanced luminol

(Perkin Elmer, Waltham, MA, USA, #NEL104001EA) and BIOMAX MR FILM (Maximum Resolution (Carestream Health Inc., Rochester, NY, USA, #870 1302).

Glycogen Colorimetric Assay

Glycogen concentration was measured using a Glycogen Colorimetric/Fluorometric Assay Kit (BioVision Inc., CA, USA, #K646-100) at 550 nm according to the manufacturer's manuals. One million cells were harvested following 48h treatment of DMSO or G9a inhibitors. Samples were homogenized with deionized water (5000 cell/µL). Denatured homogenates were centrifuged for 10 min at 15000 rpm, and supernatants were suspended with hydrolysis buffer and 50 µL were spotted in a 96-well plate. Plates were incubated for 30 min at room temperature in the presence of a reaction buffer until glycogen was measured using a Victor X4 (Perkin Elmer, Waltham, MA, USA) at 550nm. Data were normalized to cell number.

Transmission Electron Microscopy

Pellets of PF382 cells treated with DMSO, BIX01294 4 µM, UNC0638 5 µM or UNC0642 10 µM were fixed in Karnovsky solution (4% formaldehyde, 5% glutaraldehyde) for 90 minutes at room temperature. Cells were then post-fixed in 1% osmium tetroxide (OsO_4) for 90 minutes at room temperature and dehydrated by increasing concentration of alcohol. Following washing with propylene oxide, cells were embedded in epoxy resin. The fields of interest were selected on thin sections (0.5 µm) stained with methylene blue and safranin. Subsequently, ultrathin 60-80 nm thick sections were collected on a 300-mesh copper grid and stained with uranyl acetate and lead citrate. All reagents were

purchased from Sigma Aldrich, St. Louis, MO. Ultrastructural analysis of the four experimental treatments was qualitatively performed under a transmission electron microscope (Philips EM 208S, Fei Electron Optics BV, Eindhoven, Netherlands) and high-power micrographs were collected at different magnifications.

Periodic-Acid Schiff and May-Grunwald Giemsa Staining

Cyto-centrifuged (Centurion Scientific, Church Farm, Stoughton Chichester, West Sussex) treated cells were stained with a Periodic Acid Schiff (PAS) kit by using a Leica ST5020 Autostainer XL (Leica Biosystems Nussloch GmbH, Germany) or with May Grunwald reagent (Merck Millipore, #1.01425.0500). Images were obtained using an optical microscope (Leica ICC50 W, Leica Microsystem, Wetzlar, Germany).

Lysotracker detection

PF382 and SUPT1 T-ALL cell line were exposed to G9a inhibitors for 48 hours and then pulse labeled with 75 nM of the acidotropic dye LysoTracker Red DND-99 (LTRed; Invitrogen #L7528; 1 mM stock solution in DMSO) for 90 minutes at 37°C. For immunofluorescence studies, cells were centrifuged on cytospin slides and immediately analyzed on an EVOS FL fluorescence microscope (Thermo scientific, Waltham MA, USA) with a filter set at 590 nm of fluorescence emission.

Immunofluorescence

Cells were spotted on immunofluorescence slides by a cytospin centrifuge (CR2000 Small Prime Centrifuge, Centurion) and fixed for 10 min in PBS, 4% paraformaldehyde

(Thermo Fisher Scientific, Waltham MA, USA #28908) at 4°C. After 10 minutes of permeabilization in PBS, 0.4% Triton X-100 (Sigma-Aldrich, St. Louis, MO, USA, #T-9284) at room temperature, cells were blocked in PBS, 5% bovine serum albumin, 0.1% Triton X-100 and 1% goat serum (Abcam, #ab138478) for 1 hour at room temperature. The mouse monoclonal antibody against H3K9me2 (Abcam, Cambridge, United Kingdom, #ab1220) and the rabbit monoclonal antibody against G9a/*EHMT2* (Cell Signaling Technology, Danvers, MA, USA, #33065) were diluted in blocking solution and cells were incubated for 1 hour at room temperature. Alexa Fluor 488 (Invitrogen, Carlsbad, CA, USA, #A11029) and Alexa Fluor 568 (Invitrogen, Carlsbad, CA, USA, #A11036) were used as secondary antibodies and cells were stained 1 hour at room temperature protected by the light. Nuclei were stained with DAPI (Sigma-Aldrich, #D9542). Coverslips were mounted in Prolong Gold Antifade reagent (Thermo Fisher Scientific, Waltham MA, USA #P36934). Images were captured using an EVOS FL microscope (Thermo Fisher Scientific, Waltham MA, USA) and analyzed using ImageJ software (http://rsbweb.nih.gov/ij/).

Seahorse XFp Glycolytic Rate assay

The glycolysis in live cells was measured with the Seahorse XFp Glycolytic Rate Assay (Agilent Technologies, Santa Clara, CA, USA, #103346-100) and with a Seahorse XFp Analyzer (Seahorse Bioscience, North Billerica, MA) that directly measures real time extracellular acidification rates (ECAR) and oxygen consumption rate (OCR). T-ALL cells were treated with 10 μM UNC0642 for 48 hours. On the day of analysis cells were plated at 300,000 cells/well and cultured in the XFp cell culture microplate with the Seahorse

XFp RPMI medium without phenol red (#103336-100) supplemented with 10 mmol/L glucose, 1 mmol/L sodium pyruvate, 2 mmol/L glutamine, 5 mM HEPES. Cells were then incubated at 37°C in a non-CO_2 incubator for 1 hour. The entire warm medium was adjusted to pH 7.4 on the day of the assay. The initial 35 min reading recorded the basal glycolytic rate over 3 measurement periods. Next, two subsequent injections followed, comprising 0.5 µM Rotenone/ Antimycin A, Rot/AA (inhibitors of mitochondrial electron transport chain) to inhibit mitochondrial oxygen consumption (and therefore CO^2- derived protons), and 50 mM 2-deoxy-D-glucose (2-DG), a glucose analog which inhibits glycolysis. The assay data were automatically recorded and calculated by the Seahorse XFp software.

Histone PTM Quantification

PF382 and SUPT1 cells were treated with G9a inhibitors for 48 hours. Cells were counted with Trypan blue (mixed 1:1 with 50 µl of cells). For each cell line, one of the two samples were subjected to a two-step lysis procedure in which the cell pellet was suspended in a hypotonic buffer containing Nonidet NP-40 for 30 min on ice. Nuclei were pelleted, and acid extraction was performed for two hours at 4°C. The second sample was used in a one-step lysis procedure in which the cell pellet is directly suspended in the acid extraction buffer and incubated for two hours at 4°C. Cellular debris was pelleted, and lysate aliquots were frozen in a methanol-dye ice bath and stored at negative 80°C until testing. Based on higher signals, the two-step lysis method was selected for the experimental samples. Histone levels were determined by a five point 2.5-dilution series of the samples using the H3 Total bead. Multiplex assays were performed using sample volumes normalized

for H3 concentration. Beads were added to wells in 25 µl Assay Buffer supplemented with Inhibitor Cocktails (ABIC) for proteases, phosphatases and HDACs. Samples as a three-point 1.4 dilution series were added to wells in 25 µl in duplicate and incubated for 1 hour at room temperature. Three 100µl washes with 1X wash buffer (PBS containing 0.05% Tween-20) were performed using plate magnet to retain beads. 50 µl biotinylated Histone H3 antibody diluted 1:500 in assay buffer was added for the high abundance PTM multiplex assay for 1 hour with agitation. Reporter concentration for the low abundance PTM multiplex was increased twofold (1:250 dilution). Fifty µl of SAPE diluted 1:100 in assay buffer was added to each well and incubated for 30 min with agitation. Beads were collected on a plate magnet and the SAPE solution discarded. The assay plate was removed from the plate magnet and beads suspended in 100 µl 1X wash buffer and read on the Luminex MagPix instrument.

RT-PCR, RNASeq, Omni ATACSeq

RNA was extracted from PF382 cells using the RNAeasy Mini Kit as per the manufacturer's protocol (Qiagen, Hilderberg, Germany #740104). Sample quality was assessed using an agilent 2100 BioAnalyzer (Santa Clara, CA, USA). Sample libraries were prepared using NEBNext® UltraTM RNA Library Prep Kit for Illumina® (NEB, USA) following manufacturer's recommendations and index codes were added to attribute sequences to each sample and sequenced on Illumina HiSeq with paired-end 125bp/150bp to achieve an average of 40 M reads per sample at Novogene (Beijing, China). The reads were aligned to the GRCh37/hg19 human genes, and quality control tests for the aligned reads and for replicate consistency were performed by using by the

Phred score algorithm. Gene level reads and gene level expression estimate were computed as FPKM which takes into account the effects of both sequencing depth and gene length on counting of fragments(34). Differential expression between the control (DMSO) and treatment (sgRNA or UNC0642) mRNA transcripts were calculated with the union mode at HTSeq software (Novogene (Beijing, China) ranked according to signal to noise ratio (snr) (P<0.05 and Log_2 fold changes > 1.5). The GSEA v4.0.3 and transcription factor enrichment analysis TF ChEA3 softwares were used for enrichment studies. The RNA-Seq data for this study will be available for download from the Gene Expression Omnibus (GEO) repository upon manuscript publication.

ATAC sequencing was performed using the Omni-ATAC protocol as described by Corces et al.(35) 50,000 T-ALL cell lines were treated with UNC0642 for 48h and pretreated with 200 U/ml DNase prior to resuspension on RSB1 buffer (ATAC Resuspension Buffer with 0.1% NP-40, 0.1% Tween-20, 0.01% Digitonin) and subsequential wash with RSB2 buffer (ATAC Resuspension Buffer with 0.1% Tween-20). Isolated nuclei were processed for Tn5-mediated tagmentation at 37 °C for 30. Fragments were after cleaned up using a MinElute PCR purification kit (QIAGEN) and the PCR amplification was performed using NEBNext High-Fidelity 2X PCR Master Mix (NEB). The final libraries were paired end sequenced using a 75-cycle kit on a NextSeq 500 (Illumina) sequencer with a sequencing depth of 25 million reads per samples. For processing of sequencing data, samples were analyzed using the nf-core ATAC pipeline (36) that utilizes MACS2 for peak calling (37) and HOMER for annotation of peaks (38). Normalized BigWig files were scaled to 1 million mapped reads to be able to compare coverage across multiple samples. We used python

3.7.4 version and pyGenomeTracks (39) to visualize signal enrichment across the *SESN2* genomic locus.

Preclinical validation experiments in 3D cell culture

3D bioreactors, VITVO, (Rigenerand S.r.l., Medolla, Modena, Italy) were primed with 2 ml of cell culture medium to ensure a complete wetting of the 3D matrix and then loaded with $1.5x10^6$ PF382 or SUPT1 cells suspended in 1.2 ml of cell medium by a 5 ml syringe (Becton Dickinson and Co, Franklin Lakes, NJ, USA). Cells were treated 24 hours after loading at the indicated drugs concentrations. Real Time-GLO™ MT substrate was added in the medium following manufacturer instruction and luminescence was measured 2 hours after. This process has been repeated at day zero, one, two and three days after treatment and, luminescence quantified by a Victor X4 multi plate readers (Perkin Elmer, Waltham, MA, USA). Live/Dead® (Thermo Fisher Scientific, Waltham MA, USA #L3224) and Lysotracker (LTRed; Invitrogen #L7528) assays were performed three days after treatment following manufacturer instruction. 3D co-culture model of T-ALL cell lines was established growing PF382 and SUPT1 cell lines on HS-5 bone marrow stromal cell line. $0.15x10^6$ HS-5 cells were re-suspended in 1.2 ml of DMEM supplemented with 5ul/ml Hoechst (Thermo Fisher Scientific, Waltham MA, USA NucBlue™ Live ReadyProbes™ Reagent #R37605) and loaded into the VITVO inner chamber. After 24 hours devices were washed out carefully to remove Hoechst dye from the 3D cell culture and $1.5x10^6$ PF382 or SUPT1 in 1.2 ml of RPMI were loaded on HS-5 colonized scaffolds. Before treatment we waited additional 24 hours to obtain cell-cell stable interactions between stromal and T-ALL cell lines. Then, mixed cell cultures were treated with DMSO or

UNC0642 at the indicated concentrations and imaged before and 3 days after treatment for green fluorescent protein (GFP) quantification analysis. Imaging was carried out avoiding field of views with high autofluorescence of the scaffold's matrix and air bubbles. Images were captured by EVOS FL microscope (Thermo Fisher Scientific, Waltham MA, USA) using Olympus long distance 4x objective and analyzed using ImageJ software (http://rsbweb.nih.gov/ij/).

T-ALL *in Vivo* Studies

Non-obese diabetic, severe combined immune-deficient, interleukin (IL)-2 receptor gamma-deficient mice (NSG) were maintained in pathogen-free facilities at the University of Perugia. Local IACUC approved all procedures. MOLT16 T-ALL cells [2.5 x 10^6 cells in 250 µL of phosphate buffer saline (PBS)] were injected into the retro-orbital venous sinus in adult (10-12 weeks old) non-irradiated NSG mice (day of transplant was counted as day 0). *In vivo* treatment started at day 10 after transplant. Mice received UNC0642 at a dose of 5 mg/kg every 48 hours, for 12 days by intraperitoneal injection. Two mice died prematurely due to drug toxicity, leaving 7 evaluable mice in the UNC0642 treated arm and 5 in the vehicle arm. 4 x 10^6 patient derived leukemia xenograft (PDLX) T-ALLs cell, from previously established models, were injected into the retro-orbital venous sinus in adult (12-16 weeks old) sublethally-irradiated (0.9 Gy) NSG mice, 6 mice per group, males and females equally distributed among vehicle and treated arms.

PDLX-0221 received for 9 doses UNC0642 at 5 mg/kg every 48 starting 1-day post-transplant (euthanized 20 days post-transplant). The control groups received 10% DMSO (Carlo Erba Reagents S.r.l.) and 90% corn oil (Sigma-Aldrich).

Paraformaldehydes fixed organs were prepared for standard hematoxylin and eosin staining and for immunohistochemistry using human CD45 antibody (clones 2B11 + PD7/26 Dako, Agilent) and H3K9me2 (Abcam, ab#1220). Images were acquired using an Olympus BX-51 microscope (Olympus Life Science) and DM500 (Leica). The antileukemic activity of UNC0642 in PDLX (#0221) was assessed by a survival study, allowed by the short-term engraftment and immediate development of leukemia (Kaplan-Meier method), and by measuring human CD45 expression (clone HI30, BD Biosciences, New Jersey, USA) on bone marrow and peripheral blood by flow cytometry (FACS CANTO, BD Biosciences, San Jose, CA, USA).

CD1 mice were bred in the Animal Facility of the University of Parma and housed in a temperature-controlled (20–24 °C) room, under 12h light/12h dark cycle. Animal procedures were performed in accordance with European Community Directive 2010/63/UE and approved by the Ethics Committee of the University of Parma (Prot. 51/OPBA/16). 8 female mice aged between 4-6 weeks were used for the experiments. After cervical dislocation, the thymus was immediately excised, placed in a 6-well plate (Corning TM) containing 5 ml RPMI-1640 (Thermo Fisher Scientific, #MT10040CV), macroscopically separated from surrounding fat and connective tissue, and immediately used for thymocytes isolation.

Statistical Analysis and Image processing

Cell proliferation and viability data were analyzed using Graphpad PRISM software version 7 (La Jolla, CA, USA) and the Microsoft Excel Package, 2014 version (Redmond, WAS, USA). Flow cytometry data were analyzed with FlowJo analytical software version 6 or 7 (Tree Star LLC, Ashland, OR, USA).

RESULTS

G9a is a Potential Therapeutic Target in T-ALL

To identify candidate therapeutic targets in T-ALL, we evaluated inhibitors of epigenetic modifiers, including modulators of the histone acetyltransferase (HAT) p300 (CTPB and C646) and inhibitors of protein methyltransferases (PMTs), small molecules targeting EZH2 (GSK126), DOT1L (SGC0946), and G9a (*EHMT2*)/G9a-like-(GLP) (*EHMT1*) (UNC0638 and BIX01294). G9a/GLP inhibitors significantly impaired cell viability compared to the other molecules screened, as measured by the reduction of cellular ATP content, and quantified by a lower area under the curve (AUC) (Figure 1A and Supplementary Figure 1A-C). We next determined whether the effect of G9a inhibition, including with UNC0642, a second-generation derivative of UNC0638 optimized for high selectivity and *in vivo* potency against G9a and GLP (26), is more profound in the lymphoblastic lineage compared to other leukemias (e.g., myeloid) or cancer types. Indeed, analysis of the Genomics of Drug Sensitivity in Cancer database (40) or drug testing in clinical leukemia samples or cell lines revealed a preferential activity of G9a inhibitors in T-ALL compared to other tumor types (Figure 1B-C Supplementary Figure 1D-E) (IC50, BIX01294 mean = 2.52 $\pm$ 1.81 μM, 0.63<x<6.88; UNC0638 mean = 2.53 $\pm$ 1.16 μM, 1.18<x<5.03; UNC0642 mean = 3.49 $\pm$ 1.54 μM, 1.36<x<6.04).

To compare expression patterns of *EHMT2* in T-ALL to other cancers and normal cellular states, we analyzed several transcriptional databases, including the Differentiation Map (DMAP)(41), Cancer Cell Line Encyclopedia (CCLE) (42), and primary T-ALL datasets (43, 44). DMAP analysis showed a comparatively higher expression of *EHMT2* during

$CD4^+/CD8^+$ T cell lineage hematopoietic commitment (Supplementary Figure 1F) and supports the hypothesis of a preferential cancer dependency based on hematopoietic lineage commitment. T-ALL displayed higher *EHMT2*/ G9a expression compared to other tumor types (42) (Figure 1D), bone marrow cells (Figure 1E), thymocytes (Figure 1F, Supplementary Figure 1G), or lymphocytes (Figure 1G) independent from the activation of known transcription factor or recurrent mutations (Supplementary Figure 1H). G9a is consistently expressed in T-ALL cell lines, including the two spliced isoforms, long (G9a-l) and short (G9a-s) (30) (Figure 1H). Consistent with the differential distribution of G9a in normal and lymphoblasts cells, T-ALL were significantly more sensitive compared to lymphocytes (Figure 1I-J) or to $CD25^+$ thymocytes isolated from CD1 mice (Figure 1K).

G9a Blockade Alters T-ALL Proliferation, in Vitro, 3D, and Preclinical T-ALL Models

To validate G9a as a therapeutic target in T-ALL, we intersected our results with a previously published short hairpin RNA (shRNA) screen targeting nearly 350 chromatin regulator genes in DND41 T-ALL cell line models (45). *EHMT2* scored among the top 10 hits that impaired the viability of T-ALL cells (Figure 2A), indicating that T-ALL relies on *EHMT2* expression. Because shRNA-based screens are limited by the occurrence of off-target effects, we took a CRISPR approach for target validation in two validated Cas9 expressing models (PF382 and SUPT1). sgRNAs targeting the enzymatic SET domain of G9a diminished G9a expression (Figure 2B) and resulted in decreased cell viability as measured by trypan blue exclusion (Figure 2C) and an ATP-based assay (Supplementary Figure 2A) compared to a sgRNA guide (#5) targeting intronic regions (NT)

(Supplementary Figure 2B). Loss of G9a induced apoptotic cell death measured by Annexin V/propidium iodide (PI) staining (Supplementary Figure 2C).

Next, we created a 3D leukemia model (Supplementary Figure 2D) in a bioreactor device, (VITVO) (46) to recapitulate the complexity of the bone marrow microenvironment, which can impair response to small molecule therapies. Cells were treated for 72 hours with UNC0642, at 5 and 10 μM. UNC0642 treatment caused a dose-dependent decrease in T-ALL viability measured by an ATP-based assay and GFP imaging quantification (Figure 2D-E, Supplementary Figure 2E-G). We also seeded mesenchymal stromal cells (HS-5) in the inner layer of the 3D VITVO chamber and 24 hours later we loaded PF382-GFP positive cells. HS-5 cells easily attached and colonized the scaffold matrix promoting the formation of visible three-dimensional architecture with PF382 cells after 24 hours of co-culture (Figure 2F). UNC0642 treatment caused a viability defect even in the context of a leukemia-stroma interaction (Figure 2F-G), consistent with the observation that G9a inhibitors force T-ALL to undergo apoptosis (Supplementary Figure 2H).

Next, we established an orthotopic xenograft from a T-ALL cell line. After disease establishment, mice were treated for 12 days at a dose of 5 mg/kg every other day with UNC0642 versus a vehicle control by intraperitoneal injection. UNC0642 treatment resulted in a reduction of the percentage of hCD45 positive MOLT16 cells in the bone marrow of xenotransplanted mice compared to the vehicle-administered control group and, consistently, a reduction of leukemic infiltration in the spleen (Figure 2H-I). We also evaluated response in patient-derived xenograft leukemia (PDXL) models of T-ALL *in vivo*

where we demonstrated that UNC0642 reduced leukemic burden in a T-ALL PDLX model (Figure 2J).

These data credential *EHMT2* as a candidate therapeutic target in T-ALL and demonstrate that UNC0642 reduces T-ALL growth in xenograft models supporting further pre-clinical optimization of G9a chemical probes and evaluation in additional T-ALL models.

G9a Inhibition Modulates H3K9me1-2 in T-ALL

G9a primarily exerts its transcriptional silencing by targeting the mono and dimethylation of lysine-9 at histone-3 (H3K9), while methylation on H3 residues different from lysine 9 (e.g., H3K27) has been rarely described (27).

To ensure that these drugs efficiently inhibit the histone methyltransferase activity of G9a in T-ALL, we first quantified the H3K9 methyl marks (me1-3) upon acid histone extraction and found homogenous levels of methylated residues in both *NOTCH1* mutated and wild-type T-ALL cell lines (Figure 3A). Next, we performed a bead-based histone post-translational modification assay to simultaneously measure multiple histone modification targets (Figure 3B). In both PF382 and SUPT1 cell lines we observed a decrease in H3K9me2 with each of the G9a inhibitors (Figure 3C). Consistent with previous reports, UNC0642 was the more robust G9a inhibitor (29). We then analyzed acid-extracted nuclear histone fractionated proteins and whole cell lysates derived from six T-ALL cell lines treated with increasing concentrations of G9a inhibitors or the Notch Inhibitor Compound E as a negative control by western blotting, confirming a decrement of

H3K9me2 (Figure 3D, Supplementary Figure 3A-F). Furthermore, UNC0642 treatment *in vivo* modulated the H3K9me2 mark in the bone marrow and spleen of xenotransplanted mice compared to the vehicle-administered control group (Figure 3E). Consistently, sgRNA guided genetic loss of *EHMT2* caused a decrement of H3K9me2 levels (Figure 3F-I). These data support the on-target activity of both the small molecule and genetic perturbation of *EHMT2* as assessed by altered levels of H3K9me2.

G9a Loss Suppresses Sestrin2 in T-ALL

To identify pathways associated with suppression of G9a, we investigated the transcriptional consequence of G9a loss in RNA isolated from PF382 cells, expressing either non-targeting control sgRNA (sgNT), sgRNA #2 or treated with either vehicle or UNC0642. We performed a regression analysis on the significant differentially expressed genes, which showed high correlation between the *EHMT2* knockout and UNC0642 treatment (R^2 = 0.78, Supplementary Figure 4A). We established a G9a signature of mRNA transcripts repressed in sgRNA #2 or UNC0642 treatment and ranked the top 50 by the signal to noise ratio (snr) (Figure 4A). G9a modulation significantly ($P < 0.05$; Log_2 fold-change $\leq$ -0.5 or $\geq$ 0.5) altered expression of 3% of transcribed genes (1448); with nearly 55.5% down-regulated and 44.5% up-regulated, supporting the notion that, depending on tumor types (47, 48), G9a mediated H3K9 methylation can both promote and suppress gene transcription. Next, we compared our G9a signature with previously reported G9a/upregulated/downregulated gene sets (GSE113493, GSE118992, GSE51512, GSE34925, GSE70914, GSE41226) using gene set enrichment analysis (GSEA) (49). G9a transcriptional changes were significantly enriched in G9a-modulated

gene sets ($P < 0.01$, false discovery rate < 0.05) (Supplementary Figure 4B), suggesting a set of genes similarly regulated by G9a across different cancer types. To identify genes that contributed most strongly to the *EHMT2* gene sets, we applied leading edge analysis (49) to the G9a signatures (Supplementary Figure 4C) and transcription factor (TF) enrichment analysis (TFEA), a method (Figure 4B) that prioritizes transcription factors based on the overlap between a given list of differentially expressed genes, and previously annotated TF targets assembled from multiple resources (50). Both algorithms identified sestrin2 (*SESN2*) as a potential target of *EHMT2.* Consistently, we observed less accessibility at the promoter locus of *SESN2* in PF382 and SUPT1 cell lines after UNC0642 treatment, suggestive of G9a regulating transcription of *SESN2* (Figure 4C). Interestingly, *SESN2* was identified in gene ontology (GO) pathways linked to cellular stress, such as the “PERK-mediated unfolded protein response” (GO:0036499; 6 counts; adj. P = 8.868987e-05), “response to endoplasmic reticulum stress” (GO:0034976; 16 counts; adj. P = 8.868987e-05), “intrinsic apoptotic signaling pathway in response to endoplasmic reticulum stress” (GO:0070059; 8 counts; adj. P = 2.588436e-04), “cellular response to starvation” (GO:0009267; 10 counts; adj. P = 1.161513e-03) (Supplementary Figure 4D). These results suggest that G9a loss may sensitize cells to the activation of cell death and stress/autophagic related pathways.

To validate our transcriptional data, we repressed G9a catalytic activity (Figure 4D and Supplementary Figure 4E), or expression (Figure 4E), and demonstrated that *EHMT2*/G9a inactivation caused a decrement in sestrin2 expression in multiple T-ALL cell lines. Because sestrin2 is a stress induced protein involved in different cellular

adaptive responses by regulating ER stress, inflammation and autophagy (51), we decided to explore the contribution of *SESN2* repression to the phenotypic changes caused by G9a suppression.

G9a Modulates Glycolysis Rate in T-ALL

Several studies suggest that sestrin2 inhibition leads to a significant decrease of ATP cellular levels (52, 53) and aggravates stress induced death pathways associated with glucose starvation and the inhibition of glycolysis (53). First, we genetically suppressed *SESN2* (Supplementary Figure 5A) and demonstrated, T-ALL cells undergo apoptosis similarly (Supplementary Figure 5B) to T-ALL cells lacking G9a (Supplementary Figure 2C).

Next, we investigated the consequences of G9a/SESN2 axis inhibition on glycolysis using the Agilent Seahorse XFp assay. In this assay, the glycolytic rate is evaluated by measuring, in real time, the Extracellular Acidification Rate (ECAR). ECAR correlates with the conversion of glucose to lactate, which results in the net production of protons that exit the cells. Because mitochondrial respiration contributes to the acidification of the cell medium by producing CO_2 (which is partially hydrated in the extracellular medium), the Proton Efflux Rate (PER, a measurement of the extracellular acidification rate) was obtained both under basal condition and following inhibition of the mitochondrial function by rotenone and antimycin A (Rot/AA). The contribution of mitochondria/CO_2 to extracellular acidification was subtracted from PER to obtain the glycoPER which is the rate of protons extruded in the extracellular medium during glycolysis (Supplementary Figure 5C).

Basal and compensatory glycolysis rates (i.e., glycolysis rate measured following mitochondrial inhibition) were higher in vehicle versus UNC0642, UNC0638, and BIX01294 treated cells (Figure 5A, Supplementary Figure 5D) or *SESN2* knock out cells (Figure 5B) suggesting that G9a inhibition decreases the glycolytic flux in T-ALL.

We observed a trend toward a lower glycoPER in UNC0642 treated (Figure 5C) or *SESN2* deprived T-ALL cells (Figure 5D) versus DMSO or non-targeting shRNA, confirming a decrease in overall glycolysis following G9a inhibition. Consistent with this, vehicle controls had higher oxygen consumption rate (OCR) compared to UNC0642 treated (Figure 5E), or *SESN2* knock out PF382 cells (Figure 5F) indicating that G9a inhibition may also negatively affect the rate of mitochondrial respiration and therefore the capability of the cells to compensate for the inhibition of glycolysis with an increase of the oxidative phosphorylation. Collectively these data suggest a role of G9a in the control of cellular energy metabolism at least in part mediated by sestrin2 as demonstrated in the gene signature analysis, immunoblot assays and chromatin accessibility at the *SESN2* promoter locus following G9a suppression.

A consequence of defective glycolysis and ATP depletion is the feedback activation of the AKT pathway energy sensors AMP-activated protein kinase (AMPK) (54) and, ultimately, the inactivation of the glycogen synthase kinase 3 (*GSK-3A/B*) (55). GSK-3 regulates the activity of Glycogen Synthase (GS), an enzyme that mediates the conversion of glucose to glycogen. GSK-3 consists of two serine-threonine kinase α and

β paralogues and is involved in several cellular processes (56-58). GSK-3 is constitutively active in resting cells; phosphorylation at GSK-3β/α Y216/279 is activating and phosphorylation at GSK-3β/α S9/21 is inhibitory. Lysates from G9a knockout cells showed an increase in phosphorylation in GSK-3β/α S9/21 (Figure 5G) inhibitory sites with a preferential effect on GSK-3α (Supplementary Figure 5E). Similarly, lysates from G9a inhibitor treated cells revealed similar changes in the phosphorylation levels of the GSK-3β/α S9/21 sites, consistent with the inhibition of GSK-3 kinase activity (Figure 5H and Supplementary Figure 5F). Because GSK-3 inhibition has been previously shown to increase cellular glycogen content (58), we asked whether G9a inhibitor treated cells displayed glycogen accumulation in T-ALL. G9a inhibition leads to an accumulation of Periodic Acid-Schiff (PAS) positive complexes (Figure 5J), glycogen-rich electron-dense bodies in autophagosomes (Ap) (Supplementary Figure 5G), and results in the net accumulation of glycogen (Figure 5K and Supplementary Figure 5H).

Taken together, these data suggest that G9a-loss is critical to the survival of T-ALL by controlling cellular energy metabolism.

G9a Suppression Triggers Autophagy in T-ALL

G9a modulation has been reported to induce a variety of phenotypic changes in a cell context dependent manner (32) and, among the most consistent, G9a inhibition promotes autophagy-associated apoptosis (47, 59). Because glycogen accumulation leads to altered autophagosomes and lysosomes fusion or degradation (60), we asked whether the metabolic consequences of G9a suppression may alter autophagy in T-ALL.

Transmission electron microscopy (TEM) analysis showed an accumulation of autophagic vesicles in apoptotic PF382 cells (Supplementary Figure 2C, Supplementary Figure 6A), with otherwise intact organelles (Figure 6A). Consistent with this finding May-Grunwald Giemsa (MGG) stained PF382 and SUPT1 cells treated with G9a inhibitors for 48 hours showed an increased accumulation of vacuoles in the cytoplasm relative to DMSO control treatment (Figure 6B). To biochemically validate our ultra-structural analysis, we demonstrated that all three G9a inhibitors cause a dose-dependent increase in the microtubule-associated light chain 3 (LC3) form (II) protein levels bound to autophagosomes at 48 hours post-treatment (Figure 6C). These effects were not seen in T-ALL treated with chemotherapy or targeted agents (Supplementary Figure 6B-C).

In addition to autophagosomes, identified by the presence of a double membrane, TEM analysis revealed an increased number of lysosomes (Supplementary Figure 6D).

To provide further evidence of induction of autophagy by G9a inhibitors in T-ALL cells, we performed acidotropic staining with LysoTracker Red dye and observed a significant increase in the number of acidic vesicles, indicative of autophagosome/lysosome fusion in cell lines (Figure 6D), a process reverted with the addition of Bafilomycin A1 a known inhibitor of autophagosomes and lysosome fusion (Supplementary Figure 7A). Similarly, G9a inhibition triggered autophagy in cells growing in 3D matrices (Supplementary Figure 7B-E). Furthermore, genetic suppression of G9a levels (Figure 6E) caused the formation of autophagic acidotropic vesicles in T-ALL cell lines (Figure 6F). Because glycogen accumulation may result in disruptive autophagosomes and lysosomes

formation/degradation cycle (61) we repeated the acidotropic staining in the presence or absence of 2-Deoxy-d-glucose (2-DG) to lock the activity of hexokinase and inhibit the access of glucose for glycolysis and glycogen formation. As shown in Supplementary Figure 7F the addition of 2-DG rescues the autophagosome formation suggesting that the accumulation of glycogen is partially responsible for the observed phenotype in G9a treated cells.

The next question was to determine whether sestrin2 repression plays a role in the autophagy observed with G9a loss. We therefore in genetically suppressed *SESN2* and demonstrated that in *SESN2* deficient cells (Supplementary Figure 5A) the lysotracker probe accumulates in acidotropic vesicles (Figure 6G), similarly to T-ALL cells lacking G9a.

DISCUSSION

Following the recent success of inhibitors of DNA methyltransferases (DNMTs) and histone deacetylases (HDACs), some of which are now clinically approved (62), a new wave of epigenetic targeting molecules focused on histone methyltransferase inhibitors have entered clinical investigation. DOT1L, EZH2, and LSD1 inhibitors are currently being evaluated in clinical trials with evidence of therapeutic activity (63), underscoring their promise as anti-cancer agents.

We credential *EHMT2*/G9a, a SET-domain containing histone methyltransferase, as a potential therapeutic target in T-ALL and focus on elucidating and linking the role of G9a inhibitors as inducers of autophagic cell death. Epigenetic control of autophagy by methyltransferases has been reported in the setting of colorectal carcinoma where the methyltransferase EZH2 inhibits several negative regulators of mTOR (mechanistic target of rapamycin [serine/threonine]) leading to inhibition of autophagy (64). Using drosophila models, Artal-Martinez de Narvajas and colleagues demonstrated that G9a binds to the promoter regions of autophagy-associated genes *LC3B*, *WIPI1*, and *DOR* and represses gene expression in a methyltransferase-dependent manner. Importantly, they showed that when T cells undergo glucose starvation, the G9a mono and di-methylation marks are removed from the promoter regions of these autophagy genes, resulting in their increased expression (65).

BIX01294, a G9a inhibitor, was identified as a chemical inducer of autophagic cell death through a chemical screen in a single engineered breast cancer cell line (66). While the

authors suggested that the mechanism was through ROS-induced autophagy, they did not provide extensive mechanistic evidence for this phenomenon. Similarly, other studies in oral squamous cell carcinoma (67) and neuroblastoma (68) have alluded to BIX01294-induced autophagy. None of these studies were done in T-ALL, however, and none explored whether this autophagic phenotype was reproducible across other G9a inhibitors or was unique to the BIX compound.

The SET domain-containing class of methyltransferase to which G9a belongs has been implicated in several metabolic diseases (69) and cellular states (70). Although a direct role for G9a in glycogen metabolism in T-ALL has not been reported before, the notion that histone methyltransferases may be involved in metabolic regulation via transcriptional modulation has been postulated (48, 71). Histone methylation and demethylation reactions depend on metabolic coenzymes like S-adenosylmethionine (SAM), flavin adenine dinucleotide (FAD) α-ketoglutarate (αKG) that are strictly connected with glycolysis and the tricarboxylic acid (TCA) cycle (72). These metabolites fuel the one-carbon metabolic pathways that, in turn, use specific amino acids, i.e., threonine, serine, glycine, and methionine as one carbon donor-unit for macromolecule synthesis and ultimately cell proliferation. Recent findings suggest, for example, that *EHMT2* depletes serine and its downstream metabolites by repressing the transcription of genes involved in their biosynthesis such as phosphoglycerate dehydrogenase (*PHGDH*), phosphoserine aminotransferase 1 (*PSAT1*), phosphoserine phosphatase (*PSPH*), and serine hydroxymethyltransferase 2 (*SHMT2*) leading to a growth arrest in cancer cell lines of different tissue origins (48). Our transcriptional analysis also suggests

a similar modulation of one-carbon metabolism pathways and the suppression of key enzymatic regulators of the serine-glycine metabolism including *PHGDH*, *PSPH, SHMT2* and methylenetetrahydrofolate dehydrogenase/cyclohydrolase (*MTHFD2*). Interestingly, suppression of the serine hydroxymethyltransferase 1 and 2 (*SHMT1-2*) inhibits the progression of T-ALL in preclinical *in vivo* models (73), suggesting the need of improvement of different strategies -selective inhibition or epigenetic based- converging on one-carbon metabolism for the treatment of T-ALL.

Our study suggests that *EHMT2* is highly expressed in T-ALL and that T-ALL do not tolerate the loss of G9a activity. In response to the reduction of the glycolysis rate, T-ALL induce autophagy for survival to avoid cell death due the metabolic exhaustion (74). Consistent with a *EHMT2/*G9a knock-out *Drosophila* model where fly stocks accumulate glycogen (75, 76), we have observed an increase in glycogen filled autophagosomes consistent with GSK-3 inhibition and derailed autophagy leading to cell apoptosis. *SESN2* contributes to these events by sustaining the inhibition of both ATP generating pathways: glycolysis and oxidative phosphorylation. Similarly, Ding and colleagues demonstrated that sestrin2 inactivation sensitizes cells to cell death associated with a rapid decline in the ATP level bypassing the canonical caspase-dependent, ROS and mTORC1-mediated apoptosis in lung adenocarcinoma models (53).

GSK-3 recently emerged as a potential therapeutic target in T-ALL (57). Tosello *et al*. demonstrated that 6-bromoindirubin-3'-oxime (BIO) inhibits GSK-3 and promotes apoptosis. They proposed that GSK-3 acts as an oncogene in T-ALL by promoting the

stabilization of proteins such as MCL1 and c-MYB and XIAP. Thus, a potential new strategy to exploit our observations will be testing the synergistic effect of G9a and GSK-3 inhibitors in T-ALL.

Poor pharmacokinetic/pharmacodynamic properties of available G9a drugs have limited their clinical development as potential HMT targets in cancer. However, promising lead compounds are emerging such as EZM8266 developed by Epizyme for sickle cell disease and DMX8.1 developed by the collaborative effort of the QIMR Berghofer Medical Research Institute and Domainex for solid tumors.

In conclusion, drawing on insights from genetic and chemical screens, these results suggest that G9a is an actionable dependency in T-ALL and provide further support for the anti-proliferative effects of suppressing G9a HMTase activity in T-ALL. Using a combination of immunocytochemical and ultrastructural analysis, we show that G9a/GLP chemical probes cause a rapid transition to late apoptosis and autophagic phenotypes in T-ALL. Importantly, we demonstrate a previously unexplored role of *EHMT2* in the control of glycogen metabolism in T-ALL, by modulating the metabolic sensor *SESN2* and highlight a need for further investigations into the role of methyltransferases in the epigenetic control of metabolism.

CONCLUSIONS

Despite remarkable improvement in the prognosis of T-ALL, the treatment of relapsed T-ALL is still challenging. The current strategy is a combination of intensive chemotherapy regimens delivered in successive phases. While this approach has extended survival of patients, most tumors will recur, and few effective drugs then limit options for treatment. Also, minimizing the toxic side effects of currently available treatments is a major issue and new strategies are urgently needed.

Given the emerging success of epigenetic *EZH2* and *DOT1L* inhibitors in hematological cancers, our approach represents one of the first strategy to modulate the epigenome in this aggressive disease. Little is known about the therapeutic value of G9a targeting in the field of T-ALL, and our data can provide a strong rationale for preclinical studies focused on this potential target, enhancing a previously unexplored role of *EHMT2* in the control of glycogen metabolism. Although, the epigenetic-metabolomics interplay that sustains cancer cell proliferation, pluripotency and resistance to therapy are far to be dissected, our study systematically informs and expands our understanding of the epigenetic control of glycogen metabolism in cancer. Excitingly, it indicates that targeting G9a in T- ALL may represent an auxiliary strategy to exhaust cells from their metabolic requirement through the alteration of a non-canonical pathways, providing translational potential.

Moreover, given that G9a inhibitors have been already developed by Epizyme for sickle cell disease, this study can potentially place for a near term clinical translation as real therapeutic opportunity supporting further clinical validation of G9a inhibitors in cancers.

REFERENCES

1. Carpenter AC, Bosselut R. Decision checkpoints in the thymus. Nat Immunol. 2010;11(8):666-73.
2. Durinck K, Goossens S, Peirs S, Wallaert A, Van Loocke W, Matthijssens F, et al. Novel biological insights in T-cell acute lymphoblastic leukemia. Exp Hematol. 2015;43(8):625-39.
3. Goldberg JM, Silverman LB, Levy DE, Dalton VK, Gelber RD, Lehmann L, et al. Childhood T-cell acute lymphoblastic leukemia: the Dana-Farber Cancer Institute acute lymphoblastic leukemia consortium experience. J Clin Oncol. 2003;21(19):3616-22.
4. Ferrando AA, Neuberg DS, Staunton J, Loh ML, Huard C, Raimondi SC, et al. Gene expression signatures define novel oncogenic pathways in T cell acute lymphoblastic leukemia. Cancer Cell. 2002;1(1):75-87.
5. Homminga I, Pieters R, Langerak AW, de Rooi JJ, Stubbs A, Verstegen M, et al. Integrated transcript and genome analyses reveal NKX2-1 and MEF2C as potential oncogenes in T cell acute lymphoblastic leukemia. Cancer Cell. 2011;19(4):484-97.
6. Van Vlierberghe P, Ferrando A. The molecular basis of T cell acute lymphoblastic leukemia. J Clin Invest. 2012;122(10):3398-406.
7. Soulier J, Clappier E, Cayuela JM, Regnault A, Garcia-Peydro M, Dombret H, et al. HOXA genes are included in genetic and biologic networks defining human acute T-cell leukemia (T-ALL). Blood. 2005;106(1):274-86.
8. Zuurbier L, Gutierrez A, Mullighan CG, Cante-Barrett K, Gevaert AO, de Rooi J, et al. Immature MEF2C-dysregulated T-cell leukemia patients have an early T-cell precursor acute lymphoblastic leukemia gene signature and typically have non-rearranged T-cell receptors. Haematologica. 2014;99(1):94-102.
9. Van Vlierberghe P, Ambesi-Impiombato A, Perez-Garcia A, Haydu JE, Rigo I, Hadler M, et al. ETV6 mutations in early immature human T cell leukemias. J Exp Med. 2011;208(13):2571-9.
10. Zhang J, Ding L, Holmfeldt L, Wu G, Heatley SL, Payne-Turner D, et al. The genetic basis of early T-cell precursor acute lymphoblastic leukaemia. Nature. 2012;481(7380):157-63.

11. Feinberg AP, Tycko B. The history of cancer epigenetics. Nat Rev Cancer. 2004;4(2):143-53.
12. Trimarchi T, Bilal E, Ntziachristos P, Fabbri G, Dalla-Favera R, Tsirigos A, et al. Genome-wide mapping and characterization of Notch-regulated long noncoding RNAs in acute leukemia. Cell. 2014;158(3):593-606.
13. Wong AK, Sealfon RSG, Theesfeld CL, Troyanskaya OG. Decoding disease: from genomes to networks to phenotypes. Nat Rev Genet. 2021.
14. Carter B, Zhao K. The epigenetic basis of cellular heterogeneity. Nat Rev Genet. 2021;22(4):235-50.
15. Huether R, Dong L, Chen X, Wu G, Parker M, Wei L, et al. The landscape of somatic mutations in epigenetic regulators across 1,000 paediatric cancer genomes. Nat Commun. 2014;5:3630.
16. Goldberg AD, Allis CD, Bernstein E. Epigenetics: a landscape takes shape. Cell. 2007;128(4):635-8.
17. Dawson MA, Kouzarides T. Cancer epigenetics: from mechanism to therapy. Cell. 2012;150(1):12-27.
18. Hogg SJ, Beavis PA, Dawson MA, Johnstone RW. Targeting the epigenetic regulation of antitumour immunity. Nat Rev Drug Discov. 2020;19(11):776-800.
19. Zhao S, Allis CD, Wang GG. The language of chromatin modification in human cancers. Nat Rev Cancer. 2021;21(7):413-30.
20. Strahl BD, Allis CD. The language of covalent histone modifications. Nature. 2000;403(6765):41-5.
21. Cao R, Wang L, Wang H, Xia L, Erdjument-Bromage H, Tempst P, et al. Role of Histone H3 Lysine 27 Methylation in Polycomb-Group Silencing. Science. 2002;298(5595):1039.
22. Shukla N, Wetmore C, O'Brien MM, Silverman LB, Brown P, Cooper TM, et al. Final Report of Phase 1 Study of the DOT1L Inhibitor, Pinometostat (EPZ-5676), in Children with Relapsed or Refractory MLL-r Acute Leukemia. Blood. 2016;128(22).
23. Stein EM, Garcia-Manero G, Rizzieri DA, Tibes R, Berdeja JG, Savona MR, et al. The DOT1L inhibitor pinometostat reduces H3K79 methylation and has modest clinical activity in adult acute leukemia. Blood. 2018;131(24):2661-9.

24. Krivtsov AV, Evans K, Gadrey JY, Eschle BK, Hatton C, Uckelmann HJ, et al. A Menin-MLL Inhibitor Induces Specific Chromatin Changes and Eradicates Disease in Models of MLL-Rearranged Leukemia. Cancer Cell. 2019;36(6):660-73 e11.
25. Issa GC, Ravandi F, DiNardo CD, Jabbour E, Kantarjian HM, Andreeff M. Therapeutic implications of menin inhibition in acute leukemias. Leukemia. 2021;35(9):2482-95.
26. Liu F, Barsyte-Lovejoy D, Li F, Xiong Y, Korboukh V, Huang X-P, et al. Discovery of an in Vivo Chemical Probe of the Lysine Methyltransferases G9a and GLP. Journal of Medicinal Chemistry. 2013;56(21):8931-42.
27. Tachibana M, Sugimoto K, Fukushima T, Shinkai Y. SET Domain-containing Protein, G9a, Is a Novel Lysine-preferring Mammalian Histone Methyltransferase with Hyperactivity and Specific Selectivity to Lysines 9 and 27 of Histone H3. Journal of Biological Chemistry. 2001;276(27):25309-17.
28. Kubicek S, O'Sullivan RJ, August EM, Hickey ER, Zhang Q, Teodoro Miguel L, et al. Reversal of H3K9me2 by a Small-Molecule Inhibitor for the G9a Histone Methyltransferase. Molecular Cell. 2007;25(3):473-81.
29. Vedadi M, Barsyte-Lovejoy D, Liu F, Rival-Gervier S, Allali-Hassani A, Labrie V, et al. A chemical probe selectively inhibits G9a and GLP methyltransferase activity in cells. Nature Chemical Biology. 2011;7:566.
30. Shankar SR, Bahirvani AG, Rao VK, Bharathy N, Ow JR, Taneja R. G9a, a multipotent regulator of gene expression. Epigenetics. 2013;8(1):16-22.
31. Huang J, Dorsey J, Chuikov S, Zhang X, Jenuwein T, Reinberg D, et al. G9a and Glp Methylate Lysine 373 in the Tumor Suppressor p53. Journal of Biological Chemistry. 2010;285(13):9636-41.
32. Lehnertz B, Pabst C, Su L, Miller M, Liu F, Yi L, et al. The methyltransferase G9a regulates HoxA9-dependent transcription in AML. Genes & Development. 2014;28(4):317-27.
33. Follini E, Marchesini M, Roti G. Strategies to Overcome Resistance Mechanisms in T-Cell Acute Lymphoblastic Leukemia. Int J Mol Sci. 2019;20(12).

34. Trapnell C, Williams BA, Pertea G, Mortazavi A, Kwan G, van Baren MJ, et al. Transcript assembly and quantification by RNA-Seq reveals unannotated transcripts and isoform switching during cell differentiation. Nat Biotechnol. 2010;28(5):511-5.
35. Corces MR, Trevino AE, Hamilton EG, Greenside PG, Sinnott-Armstrong NA, Vesuna S, et al. An improved ATAC-seq protocol reduces background and enables interrogation of frozen tissues. Nat Methods. 2017;14(10):959-62.
36. Ewels PA, Peltzer A, Fillinger S, Patel H, Alneberg J, Wilm A, et al. The nf-core framework for community-curated bioinformatics pipelines. Nat Biotechnol. 2020;38(3):276-8.
37. Zhang Y, Liu T, Meyer CA, Eeckhoute J, Johnson DS, Bernstein BE, et al. Model-based analysis of ChIP-Seq (MACS). Genome Biol. 2008;9(9):R137.
38. Heinz S, Benner C, Spann N, Bertolino E, Lin YC, Laslo P, et al. Simple combinations of lineage-determining transcription factors prime cis-regulatory elements required for macrophage and B cell identities. Mol Cell. 2010;38(4):576-89.
39. Lopez-Delisle L, Rabbani L, Wolff J, Bhardwaj V, Backofen R, Gruning B, et al. pyGenomeTracks: reproducible plots for multivariate genomic datasets. Bioinformatics. 2021;37(3):422-3.
40. Yang W, Soares J, Greninger P, Edelman EJ, Lightfoot H, Forbes S, et al. Genomics of Drug Sensitivity in Cancer (GDSC): a resource for therapeutic biomarker discovery in cancer cells. Nucleic Acids Research. 2013;41(D1):D955-D61.
41. Novershtern N, Subramanian A, Lawton LN, Mak RH, Haining WN, McConkey ME, et al. Densely Interconnected Transcriptional Circuits Control Cell States in Human Hematopoiesis. Cell. 2011;144(2):296-309.
42. Barretina J, Caponigro G, Stransky N, Venkatesan K, Margolin AA, Kim S, et al. The Cancer Cell Line Encyclopedia enables predictive modelling of anticancer drug sensitivity. Nature. 2012;483:603.
43. Liu Y, Easton J, Shao Y, Maciaszek J, Wang Z, Wilkinson MR, et al. The genomic landscape of pediatric and young adult T-lineage acute lymphoblastic leukemia. Nat Genet. 2017;49(8):1211-8.

44. Chen B, Jiang L, Zhong ML, Li JF, Li BS, Peng LJ, et al. Identification of fusion genes and characterization of transcriptome features in T-cell acute lymphoblastic leukemia. Proc Natl Acad Sci U S A. 2018;115(2):373-8.
45. Knoechel B, Roderick JE, Williamson KE, Zhu J, Lohr JG, Cotton MJ, et al. An epigenetic mechanism of resistance to targeted therapy in T cell acute lymphoblastic leukemia. Nature Genetics. 2014;46:364.
46. Candini O, Grisendi G, Foppiani EM, Brogli M, Aramini B, Masciale V, et al. A Novel 3D In Vitro Platform for Pre-Clinical Investigations in Drug Testing, Gene Therapy, and Immuno-oncology. Sci Rep. 2019;9(1):7154.
47. Ke XX, Zhang R, Zhong X, Zhang L, Cui H. Deficiency of G9a Inhibits Cell Proliferation and Activates Autophagy via Transcriptionally Regulating c-Myc Expression in Glioblastoma. Front Cell Dev Biol. 2020;8:593964.
48. Ding J, Li T, Wang X, Zhao E, Choi J-H, Yang L, et al. The Histone H3 Methyltransferase G9A Epigenetically Activates the Serine-Glycine Synthesis Pathway to Sustain Cancer Cell Survival and Proliferation. Cell metabolism. 2013;18(6):10.1016/j.cmet.2013.11.004.
49. Subramanian A, Tamayo P, Mootha VK, Mukherjee S, Ebert BL, Gillette MA, et al. Gene set enrichment analysis: a knowledge-based approach for interpreting genome-wide expression profiles. Proc Natl Acad Sci U S A. 2005;102(43):15545-50.
50. Keenan AB, Torre D, Lachmann A, Leong AK, Wojciechowicz ML, Utti V, et al. ChEA3: transcription factor enrichment analysis by orthogonal omics integration. Nucleic Acids Res. 2019;47(W1):W212-W24.
51. Wang LX, Zhu XM, Yao YM. Sestrin2: Its Potential Role and Regulatory Mechanism in Host Immune Response in Diseases. Front Immunol. 2019;10:2797.
52. Ben-Sahra I, Dirat B, Laurent K, Puissant A, Auberger P, Budanov A, et al. Sestrin2 integrates Akt and mTOR signaling to protect cells against energetic stress-induced death. Cell Death Differ. 2013;20(4):611-9.
53. Ding B, Parmigiani A, Divakaruni AS, Archer K, Murphy AN, Budanov AV. Sestrin2 is induced by glucose starvation via the unfolded protein response and protects cells from non-canonical necroptotic cell death. Sci Rep. 2016;6:22538.

54. Hardie DG. The AMP-activated protein kinase pathway--new players upstream and downstream. J Cell Sci. 2004;117(Pt 23):5479-87.
55. Frame S, Cohen P, Biondi RM. A common phosphate binding site explains the unique substrate specificity of GSK3 and its inactivation by phosphorylation. Mol Cell. 2001;7(6):1321-7.
56. Banerji V, Frumm SM, Ross KN, Li LS, Schinzel AC, Hahn CK, et al. The intersection of genetic and chemical genomic screens identifies GSK-3alpha as a target in human acute myeloid leukemia. J Clin Invest. 2012;122(3):935-47.
57. Tosello V, Bordin F, Yu J, Agnusdei V, Indraccolo S, Basso G, et al. Calcineurin and GSK-3 inhibition sensitizes T-cell acute lymphoblastic leukemia cells to apoptosis through X-linked inhibitor of apoptosis protein degradation. Leukemia. 2016;30(4):812-22.
58. Wagner FF, Benajiba L, Campbell AJ, Weiwer M, Sacher JR, Gale JP, et al. Exploiting an Asp-Glu "switch" in glycogen synthase kinase 3 to design paralog-selective inhibitors for use in acute myeloid leukemia. Sci Transl Med. 2018;10(431).
59. De Smedt E, Devin J, Muylaert C, Robert N, Requirand G, Vlummens P, et al. G9a/GLP targeting in MM promotes autophagy-associated apoptosis and boosts proteasome inhibitor-mediated cell death. Blood Adv. 2021;5(9):2325-38.
60. van der Ploeg AT, Reuser AJ. Pompe's disease. Lancet. 2008;372(9646):1342-53.
61. Spampanato C, Feeney E, Li LS, Cardone M, Lim JA, Annunziata F, et al. Transcription factor EB (TFEB) is a new therapeutic target for Pompe disease. Embo Mol Med. 2013;5(5):691-706.
62. Arrowsmith CH, Bountra C, Fish PV, Lee K, Schapira M. Epigenetic protein families: a new frontier for drug discovery. Nature Reviews Drug Discovery. 2012;11:384.
63. Morera L, Lübbert M, Jung M. Targeting histone methyltransferases and demethylases in clinical trials for cancer therapy. Clinical Epigenetics. 2016;8:57.
64. Wei F-Z, Cao Z, Wang X, Wang H, Cai M-Y, Li T, et al. Epigenetic regulation of autophagy by the methyltransferase EZH2 through an MTOR-dependent pathway. Autophagy. 2015;11(12):2309-22.

65. Artal-Martinez de Narvajas A, Gomez TS, Zhang J-S, Mann AO, Taoda Y, Gorman JA, et al. Epigenetic Regulation of Autophagy by the Methyltransferase G9a. Molecular and Cellular Biology. 2013;33(20):3983-93.
66. Kim Y, Kim Y-S, Kim DE, Lee JS, Song JH, Kim H-G, et al. BIX-01294 induces autophagy-associated cell death via EHMT2/G9a dysfunction and intracellular reactive oxygen species production. Autophagy. 2013;9(12):2126-39.
67. Ren A, Qiu Y, Cui H, Fu G. Inhibition of H3K9 methyltransferase G9a induces autophagy and apoptosis in oral squamous cell carcinoma. Biochemical and Biophysical Research Communications. 2015;459(1):10-7.
68. Ke X-X, Zhang D, Zhu S, Xia Q, Xiang Z, Cui H. Inhibition of H3K9 Methyltransferase G9a Repressed Cell Proliferation and Induced Autophagy in Neuroblastoma Cells. PLoS ONE. 2014;9(9):e106962.
69. El-Osta A, Brasacchio D, Yao D, Pocai A, Jones PL, Roeder RG, et al. Transient high glucose causes persistent epigenetic changes and altered gene expression during subsequent normoglycemia. The Journal of Experimental Medicine. 2008;205(11):2683-.
70. Chen H, Yan Y, Davidson TL, Shinkai Y, Costa M. Hypoxic stress induces dimethylated histone H3 lysine 9 through histone methyltransferase G9a in mammalian cells. Cancer Res. 2006;66(18):9009-16.
71. Teperino R, Schoonjans K, Auwerx J. Histone Methyl Transferases and Demethylases; Can They Link Metabolism and Transcription? Cell Metabolism. 2010;12(4):321-7.
72. Ducker GS, Rabinowitz JD. One-Carbon Metabolism in Health and Disease. Cell Metab. 2017;25(1):27-42.
73. Pikman Y, Ocasio-Martinez N, Alexe G, Dimitrov B, Kitara S, Diehl FF, et al. Targeting serine hydroxymethyltransferases 1 and 2 for T-cell acute lymphoblastic leukemia therapy. Leukemia. 2021.
74. Kawaguchi M, Aoki S, Hirao T, Morita M, Ito K. Autophagy is an important metabolic pathway to determine leukemia cell survival following suppression of the glycolytic pathway. Biochemical and Biophysical Research Communications. 2016;474(1):188-92.

75. Riahi H, Brekelmans C, Foriel S, Merkling SH, Lyons TA, Itskov PM, et al. The histone methyltransferase G9a regulates tolerance to oxidative stress-induced energy consumption. PLoS Biol. 2019;17(3):e2006146.
76. An PNT, Shimaji K, Tanaka R, Yoshida H, Kimura H, Fukusaki E, et al. Epigenetic regulation of starvation-induced autophagy in Drosophila by histone methyltransferase G9a. Sci Rep. 2017;7(1):7343.

FIGURE LEGENDS

Figure 1: T-ALL cells are dependent on *EHMT2*

A) Effect of epigenetic modulators BIX01294, C646, CTPB, GSK126, SGC0946, and UNC0638 in T-ALL cell lines (ALL/SIL, CCRF-CEM, DND41, HPB-ALL, HSB2, and PEER). BIX01294 is a diazepin-quinazolin-amine derivative that selectively inhibits the H3K9 di-methylation activity of G9a, and to a lesser extent GLP, without competing for the S-adenosyl-methionine (SAM) cofactor [15]; C646 is a selective small molecule inhibitor of histone acetyltransferase p300; CTPB is an amide derivative that selectively activates the histone acetyltransferase (HAT) p300; GSK126 is a EZH2 methyltransferase inhibitor; GC0946 is a highly potent and selective DOT1L methyltransferase inhibitor; UNC0638 is a substrate-competitive small-molecule inhibitor with equal potency for G9a and GLP in cell-based assays[16]. The scatter dot plot represents the effect of small molecules on cellular viability calculated using the area under the curve (AUC) model of log transformed dose-response data using GraphPad V7. A lower AUC corresponds to a greater sensitivity.

B) Graph showing response to the G9a inhibitor, UNC0638, in over 900 cancer cell lines screened as part of the Genomics of Drug Sensitivity in Cancer Project (GDS). T-ALL cell lines are indicated in red, non-T-ALL cell lines in gray. Statistical significance among groups (****$P \leq 0.0001$) was determined by a non-parametric t-test (Mann-Whitney).

C) Effect of epigenetic modulators BIX01294, UNC0638, UNC0642 in T-ALL (n=10), AML (n=5) cell lines and primary patients T-ALL cells (n=4) and primary patients AML cells (n=4) samples. The scatter dot plot represents the effect of small molecules on cellular viability calculated using the area under the curve (AUC) model of log transformed dose-response (BIX01294=0<[X]<8 μM; UNC038=0<[X]<10 μM; UNC042=0<[X]<10 μM) data using GraphPad V7. A lower AUC corresponds to a greater sensitivity. Statistical significance among groups (**$P \leq 0.01$) was determined by a non-parametric t-test (Mann-Whitney).

(D) *EHMT2* expression levels in 36 cancer types (1036 cancer cell lines). Data were obtained from the Cancer Cell Line Encyclopedia (42). A red bar represents the T-ALL cell lines.

(E) *EHMT2* expression levels in normal bone marrow cells (n=6) or in T-ALL lymphoblasts (n=11). Data were obtained from the Anderson leukemia data set (PMID:15068665). The line in the box-and-whisker diagram represents the Log_2 median centered ratio. The upper edge (hinge) of the box indicates the 75^{th} percentile of the data, and the lower hinge the 25^{th} percentile. The whiskers represent the minimum and the maximum data values. Statistical significance among groups (*$P \leq 0.05$) was determined by a non-parametric t-test (Mann-Whitney).

(F) G9a and H3K9me2 expression in murine thymus and T-ALL lymphoblasts. Formalin-fixed, paraffin embedded tissue sections were stained with anti G9a and anti H3K9me2. Scale bars, 20 μm. Hassall's corpuscles are indicated by arrowheads.

(G) *EHMT2* expression levels in lymphocytes (n=5) or in T-ALL lymphoblasts (n=33). The line in the box-and-whisker diagram represents the Log_2 *EHMT2* median expression calculated according to the $\Delta\Delta$CT method. The upper edge (hinge) of the box indicates the 75th percentile of the data, and the lower hinge the 25th percentile. The end of the vertical line represents the minimum and the maximum data values. Statistical significance among groups (*$P \leq 0.05$) was determined by a non-parametric t-test (Mann-Whitney).

(H) Western immunoblotting showing expression of G9a (l=long isoform; s=short isoform), GLP, and ICN1 in a panel of T-ALL cell lines. GAPDH was used as a loading control.

(I) Effect of G9a inhibitors BIX01294, UNC0638, and UNC0642 in primary T-ALL blasts (n=3) or isolated lymphocytes (n=6). Cells were grown at increasing concentrations of G9a/GLP inhibitors (BIX01294, UNC0638, and UNC0642) and viability evaluated at day 3 by an ATP-based assay and plotted as the percentage of viable cells relative to a DMSO control. Shown is the mean ± standard deviation (SD) of a minimum of two replicates.

(J) Effect of the G9a inhibitors BIX01294, UNC0638, and UNC0642 in primary T-ALL cells (n=3) or isolated lymphocytes (n=6). The scatter dot plot represents the effect of small

molecules on cellular viability calculated using the AUC model of log transformed dose-responses data using GraphPad V7. The line in the box-and-whisker diagram represents the AUC median. The upper edge (hinge) of the box indicates the 75th percentile of the data, and the lower hinge the 25th percentile. The ends of the vertical line indicate the minimum and the maximum data values. Statistical significance (*$P \leq 0.05$) was determined by a non-parametric t-test (Mann-Whitney).

(K) Effect of G9a inhibitors BIX01294, UNC0638, and UNC0642 in CD25^{+} thymic cells isolated from CD1 mice or PDLX T-ALL cells. Cells were grown at increasing concentrations of G9a/GLP inhibitors (BIX01294, UNC0638, and UNC0642) and viability evaluated at day 3 by an ATP-based assay and plotted as the percentage of viable cells relative to a DMSO control. Shown is the mean ± standard deviation (SD) of a minimum of two replicates.

Figure 2: G9a enzymatic abrogation impairs T-ALL proliferation *in vitro*, 3D *and in vivo* preclinical T-ALL models

(A) shRNA screen identified that *EHMT2* is required for T-ALL cell survival. Top hits are ranked with a negative Normalized Enrichment Score (NES). shRNA screen was performed in DND41 (45).

(B) Schematic representation of the G9a protein with the indicated functional domains (top). On the bottom, western immunoblotting showing expression of G9a in PF382 and

SUPT1 cells 2 days post sgRNA selection. Protein lysates were stained with an anti-G9a antibody. GAPDH was used as loading control. NT=non-targeting.

(C) Effect of G9a loss in PF382 and SUPT1 cells at four or six days post sgRNA selection. Histograms show cell count using the trypan blue exclusion assay. Error bar denotes the mean ± SD of a minimum of three biological replicates. Statistical significance among groups (****$P \leq 0.0001$) was determined by a non-parametric t-test (Mann-Whitney). NT=non-targeting, #2 = sgRNA #2 directed against *EHMT2*.

(D) Live Dead assay of GFP+ PF382 in 3D cell culture treated with DMSO or UNC0642 at the indicated concentrations. Representative immunofluorescence images of control or UNC0642 treated PF382 cells upon Live/Dead® staining at 72 hours. Scale bars: 1000 µm.

(E) Cell viability assay of GFP+ PF382 cell in 3D culture treated with DMSO or UNC0642 at the indicated concentrations. Cell death is indicated in the histogram as a fluorescence ratio between GFP+ (viable cells) and RFP+ (dead cells) signals of the acquired fields. Error bars denote the mean ± standard deviation (SD) of one representative experiment. Statistical significance among groups for treated vs. vehicle (DMSO) (****$P \leq 0.0001$) was determined by one-way ANOVA using Bonferroni's correction for multiple comparison testing.

(F) Preclinical validation of UNC0642 in PF382 co-cultured with HS-5 human stromal cells in 3D scaffolds. Representative immunofluorescence images of control or UNC0642 treated PF382 (green) cultured in 3D scaffolds with stromal HS-5 cells (blue) at Day 3. Scale bars: 1000 μm.

(G) Preclinical validation of UNC0642 in PF382 co-cultured with HS-5 human stromal cells in 3D scaffolds. The histogram shows the effect of UNC0642 treatment on PF382 cell viability as represented by a GFP fold increase relative to day 1. Error bars denote the mean ± standard deviation (SD) of one representative experiment. Statistical significance among groups for treated vs. vehicle (DMSO) (*$P \leq 0.05$) was determined by one-way ANOVA using Bonferroni's correction for multiple comparison testing. For image quantification, we selected fields with minor autofluorescence of the scaffold's matrix and no air bubbles.

(H) Antileukemic activity of UNC0642 in hCD45+ bone marrow infiltrating cells (top panels) and spleen (bottom panel) in a MOLT16 xenografted murine model after 12 days of UNC0642 treatment (5 mg/kg/IP every 48 hours) or vehicle (corn oil).

(I) The number of hCD45+ cells per field was represented as percentage relative to vehicle control. Error bars denote the mean ± SD of 8 fields from 3 representative mice treated with UNC0642 or the mean ± SD of 3 fields from 3 representative vehicle treated mice. Statistical significance for treated vs. vehicle (*$P \leq 0.05$, **$P \leq 0.01$) was determined by non-parametric t-test (Mann-Whitney).

(J) Antileukemic activity of UNC0642 in hCD45+ T-ALL leukemia cells (bone-marrow and peripheral cells T-ALL lymphoblasts) in a PDLX T-ALL murine model after 9 days of UNC0642 treatment (5 mg/kg/IP every 48 hours) or vehicle (corn oil). Statistical significance for treated vs. vehicle ($*P \leq 0.05$) was determined by non-parametric t-test (Mann-Whitney). On the right Kaplan–Meier survival plots showing the overall survival (OS) of PDLX T-ALL mice treated or untreated with UNC0642 (5 mg/kg/IP every 48 hours) ($**P \leq 0.01$).

Figure 3: G9a inhibitors reduce H3K9me2 level in T-ALL

(A) Western immunoblotting showing expression of H3K9me1, H3K9me2, and H3K9me3 in a panel of T-ALL cell lines. An acidic histone protein extraction was performed. Total histone 3 (H3) was used as a loading control.

(B) Schematic representation of the histone protein methyltransferase, Luminex beads assay. The beads/target panel included H3K9me1, H3K9me2, H3K9me3, H3K27ac, H3K27me2, H3K27me3, and H3K36me3.

(C) Luminex PMT assay. Lysates were obtained from acidic extraction upon 48 hours treatment with the indicated concentrations of G9a inhibitors. Histograms show the median fluorescence intensity of each histone mark normalized to the intensity of total H3. Detection was repeated three times by diluting initial protein concentration with a 2.5-

dilution series. Graphs are representative of one out of three Luminex quantifications. Red bar indicates H3K9me2 loss.

(D) Western immunoblotting showing expression of H3K9me2 in PF382 and SUPT1 cells treated at the indicated concentrations of G9a inhibitors for 48 hours. Protein lysates were obtained using an acidic histone extraction protocol and stained with an antibody recognizing the H3K9me2 residue or total H3 used as a loading control.

(E) Modulation of H3K9me2 in xenografted murine models after 12 days (X-MOLT16), 26 (PDLX-0121), 9 (PDLX-0122) of UNC0642 treatment (5 mg/kg/IP every 48 hours) or vehicle (corn oil). Top panel=bone morrow, bottom panel=spleen. Scale bar: 20 μm.

Effect of *EHMT2* knockout on H3K9me2 in PF382 cells two days post sgRNA selection. Immunofluorescence of permeabilized PF382 cells stained with anti-G9a (red) (F) and H3K9me2 (green) (H) is shown. Cell nuclei were stained with DAPI (blue). Scale bar: 100 μm. NT=non-targeting, #2 =sgRNA #2 directed against *EHMT2*.

Quantitative immunofluorescence analysis of G9a/EHMT2 (G) and H3K9me2 (I) nuclear signal in PF382 cells after two days post sgRNA selection. Error bars denote the mean ± standard deviation (SD) of fluorescence of single nucleus (arbitrary units); Statistical significance among NT vs. sgRNA #2 was determined by unpaired t-test (***$P \leq 0.001$).

Figure 4: Transcriptional consequences of G9a loss in T-ALL

(A) Heatmap showing mRNA expression of differentially expressed genes in non-targeting sgRNA (sgNT), sgRNA targeting *EHMT2* (#2) or T-ALL cells treated either with vehicle or UNC0642 ($P < 0.05$ and Log_2 fold changes > 1.5) and ranked for signal to noise ratio (snr).

(B) Clustergram showing transcription factor enrichment analysis (TFEA). G9a loss gene set from (A) was compared to ChEA3 libraries of TF target gene sets assembled from multiple orthogonal 'omics' datasets as listed in https://amp.pharm.mssm.edu/chea3/#top. Red boxes show the overlapping query gene targets among top library results.

(C) Chromatin accessibility across the *SESN2* locus. Genome tracks show accessible loci across the *SESN2* locus chr1:28544312-2862776 based on Assay for Transposase-Accessible Chromatin (omni-ATAC) sequencing data of 2 technical replicates for PF382 cells and SUPT1 cells after 48h of UNC0642 treatment (reds) and DMSO (blue). The bottom bar represents the genes (hg19).

(D) Western immunoblotting showing expression of sestrin2 in PF382 cells treated at the indicated concentrations of G9a inhibitors after 48 hours. Actin was used as a loading control.

(E) Western immunoblotting showing expression of G9a/EHMT2, sestrin2, H3K9me2, and H3 Total, in PF382 cells after two days post sgRNA selection. HSP90 was used as a loading control. NT= non targeting; #2 = sgRNA #2 directed against *EHMT2*.

Figure 5: EHMT2 Modulates Glycogen Synthase Kinase 3 (GSK-3) in T-ALL

(A) Glycolytic phenotype in PF382 cells. Histograms represent mean ± SD of three replicates of PF382 T-ALL cells treated with DMSO, BIX01294 (2 μM), or UNC0638 (5 μM) or UNC0642 (10 μM) on the x-axis. The y-axis represents the glycolytic proton efflux rate (PER) at the basal and compensatory level. Statistical significance among groups (*P < 0.05, **P < 0.01) was determined by a non-parametric t-test (Mann-Whitney).

(B) Glycolytic phenotype in *SESN2* knockout PF382 cells. Histograms represent mean ± SD of three replicates of *SESN2* deprived T-ALL cells. The y-axis represents the glycolytic proton efflux rate (PER) at the basal and compensatory level. Statistical significance among groups (*P < 0.05, ***P < 0.001) was determined by a non-parametric t-test (Mann-Whitney).

(C) Time resolved glycolytic proton efflux rate (glycoPER). Traces represent the mean ± SD of three replicates of PF382 cells treated with DMSO or UNC0642 analyzed over 70-minute time course experiments. Statistical significance among groups for treated vs. vehicle (DMSO) (*P < 0.05; **P < 0.01, ***P < 0.001, ****P < 0.0001) was determined by two-way ANOVA using Bonferroni's correction for multiple comparison testing.

(D) Time resolved glycolytic proton efflux rate (glycoPER). Traces represent the mean ± SD of three replicates of *SESN2* knockout PF382 analyzed over 70-minute time course experiments. Statistical significance among groups for treated vs. vehicle (DMSO) (*P < 0.05) was determined by two-way ANOVA using Bonferroni's correction for multiple comparison testing.

(E) Oxygen Consumption Rate (OCR). Traces represent the mean ± SD of three replicates of PF382 T-ALL cells treated with DMSO or UNC0642 analyzed over a 70-minute time course experiment. Statistical significance among groups for treated vs. vehicle (DMSO) (*P < 0.05; **P < 0.01, ***P < 0.001, ****P < 0.0001) was determined by two-way ANOVA using Bonferroni's correction for multiple comparison testing.

(F) Oxygen Consumption Rate (OCR). Traces represent the mean ± SD of three replicates of PF382 *SESN2* knockout cells analyzed over a 70-minute time course experiment. Statistical significance among groups for treated vs. vehicle (DMSO) (****P < 0.0001) was determined by two-way ANOVA using Bonferroni's correction for multiple comparison testing.

(G) Modulation of GSK-3 in PF382 and SUPT1 cells after two days post sgRNA selection. Western immunoblot showing expression phosphorylated serine-9 in GSK-3β or serine-21 in GSK-3α in T-ALL. Protein lysates were stained with G9a/*EHMT2*, P-GSK-3α (Ser21), P-GSK-3β (Ser9), GSK-3 total. NT=non-targeting. NT=non-targeting, #2 = sgRNA #2 directed against *EHMT2*. See Figure 5E for *EHMT2* knock out level.

(H) Modulation of GSK-3 by the G9a inhibitor UNC0642. Western immunoblot showing phosphorylation of serine-9 in GSK-3β or serine-21 in GSK-3α in T-ALL. Cell lysates were obtained after 48 hours of drug treatment as indicated. Protein lysates were stained with P-GSK-3α (Ser21), P-GSK-3β (Ser9), and GSK-3 Total. HSP90 was used as loading control.

(I) Western immunoblotting showing level of p-mTOR (Ser-2448), sestrin-2, and p-p70s6K in PF382 cells after UNC0642 treatment or 24 hours of GSK-3 inhibitor (SB216763 and CHIR-99021) treatment at the indicated concentration. Actin was used as a loading control.

(J) Micrographs documenting Periodic Acid Shift (PAS) staining in PF382 and SUPT1 cell lines treated with vehicle (DMSO) or the indicated doses of BIX01294, UNC0638 and UNC0642 for 48 hours. Fine dispersed granular or blocks of PAS+ (magenta) cytoplasmic and perinuclear material correspond to glycogen. Scale bars: 13 μm.

(K) Effect of G9a inhibitors BIX01294, UNC0638, and UNC0642 on cellular glycogen content. Histograms show the glycogen fold change increase relative to a DMSO control after G9a inhibitors treatment for 48 hours. Error bars denote the mean ± standard deviation (SD) of two biological replicates. Statistical significance among groups (*$P \leq 0.05$, **$P \leq 0.01$) was determined by a non-parametric t-test (Mann-Whitney).

Figure 6: G9a Suppression Triggers Apoptosis and Autophagy in T-ALL

(A) TEM micrographs illustrating the morphology of untreated (DMSO) T-ALL cells and the effects of BIX01294, UNC0638 and UNC0642. Black rectangles (upper) inscribe areas shown at higher magnification (lower) to illustrate the phases of autophagosome (Ap) formation with G9a inhibitions. Scale Bars: upper panels DMSO 1 μm, G9a inhibitors 2 μm; lower panels DMSO 0.5 μm, G9a inhibitors 1 μm.

(B) Representative images of May Grunwald-Giemsa stained cytospin preparations of T-ALL (PF382 and SUPT1) cultured in vehicle (DMSO) or BIX01294, UNC0638 or UNC0642 for 48 hours. Extensive cytoplasmic vacuolization is apparent following exposure to G9a inhibitors. Images were captured with a Leica ICC50W optical microscope (100X). Scale bars: 13 μm.

(C) Western immunoblotting showing expression of LC3B-II in PF382 and SUPT1 cells treated at the indicated concentrations of G9a inhibitors for 48 hours. HSP90 was used as a loading control.

(D) LysoTracker® Red DND-99 staining of T-ALL cells labeled treated with BIX01294, UNC0638 and UNC0642 treatment for 48h. Scale Bars: 100 μm.

(E) Western immunoblot showing expression of G9a, two days post sgRNA selection. Protein lysates were blotted with a G9a antibody, HSP90 was used as loading control. NT=non-targeting, #2 = sgRNA #2 directed against *EHMT2*.

(F) LysoTracker® Red DND-99 staining of T-ALL cells two days post sgRNA selection. Scale bar: 100 μm. NT=non-targeting, #2 = sgRNA #2 directed against *EHMT2*.

(G) LysoTracker® Red DND-99 staining of T-ALL cells two days post selection for shRNA targeting *SESN2* selection. Scale bar: 200 μm.

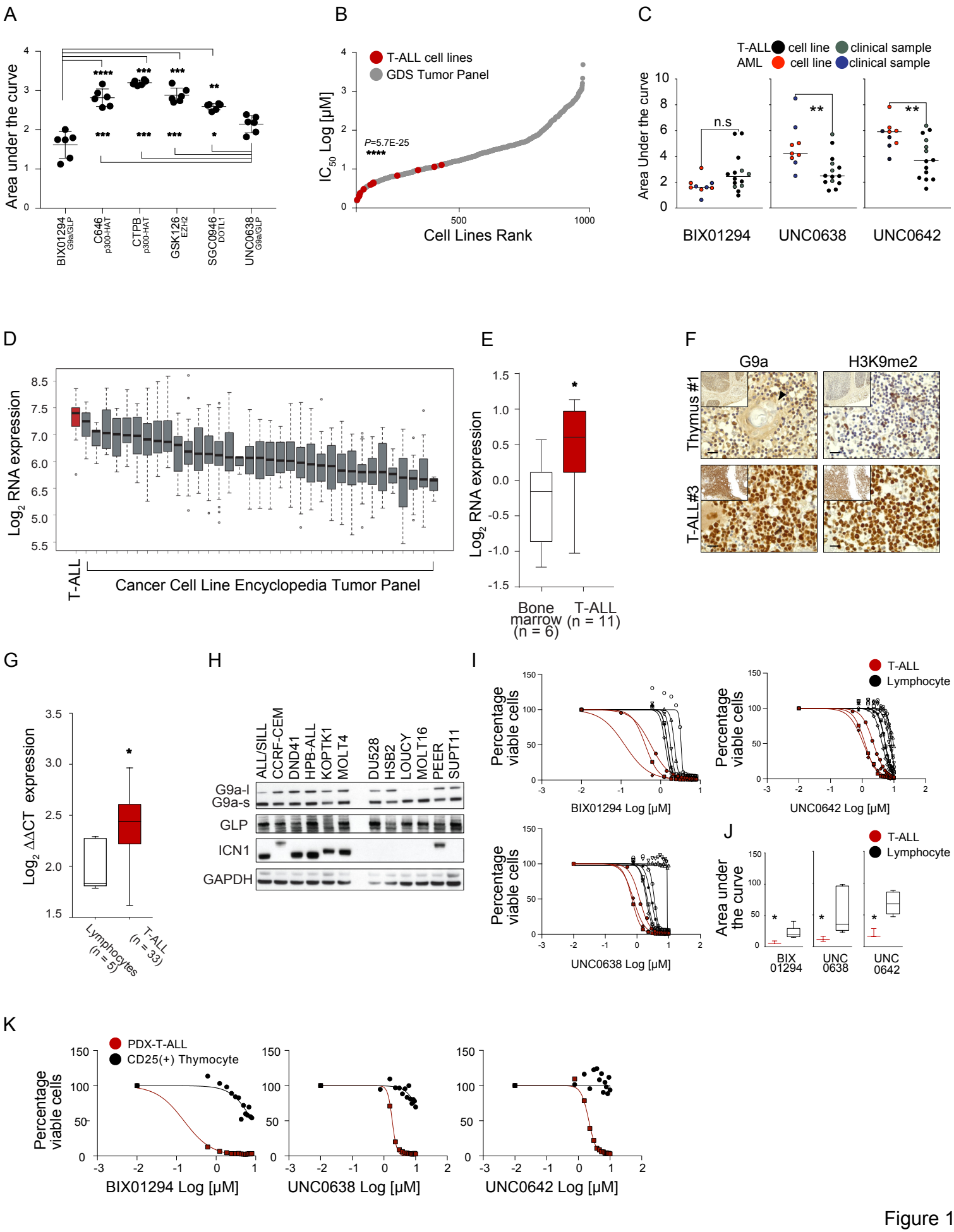
A
Area under the curve
BIX01294 G9a/GLP
C646 p300-HAT
CTPB p300-HAT
GSK126 EZH2
SGC0946 DOT1L
UNC0638 G9a/GLP
B
T-ALL cell lines
GDS Tumor Panel
P=5.7E-25
IC50 Log [µM]
Cell Lines Rank
C
T-ALL cell line
clinical sample
AML cell line
clinical sample
Area Under the curve
n.s
BIX01294
UNC0638
UNC0642
D
Log2 RNA expression
T-ALL
Cancer Cell Line Encyclopedia Tumor Panel
E
Log2 RNA expression
Bone marrow (n = 6)
T-ALL (n = 11)
F
G9a
H3K9me2
Thymus #1
T-ALL#3
G
Log2 ΔΔCT expression
Lymphocytes (n = 5)
T-ALL (n = 33)
H
ALL/SILL
CCRF-CEM
DND41
HPB-ALL
KOPTK1
MOLT4
DU528
HSB2
LOUCY
MOLT16
PEER
SUPT11
G9a-l
G9a-s
GLP
ICN1
GAPDH
I
Percentage viable cells
BIX01294 Log [µM]
UNC0642 Log [µM]
UNC0638 Log [µM]
T-ALL
Lymphocyte
J
Area under the curve
BIX 01294
UNC 0638
UNC 0642
K
PDX-T-ALL
CD25(+) Thymocyte
Percentage viable cells
BIX01294 Log [µM]
UNC0638 Log [µM]
UNC0642 Log [µM]

Figure 1

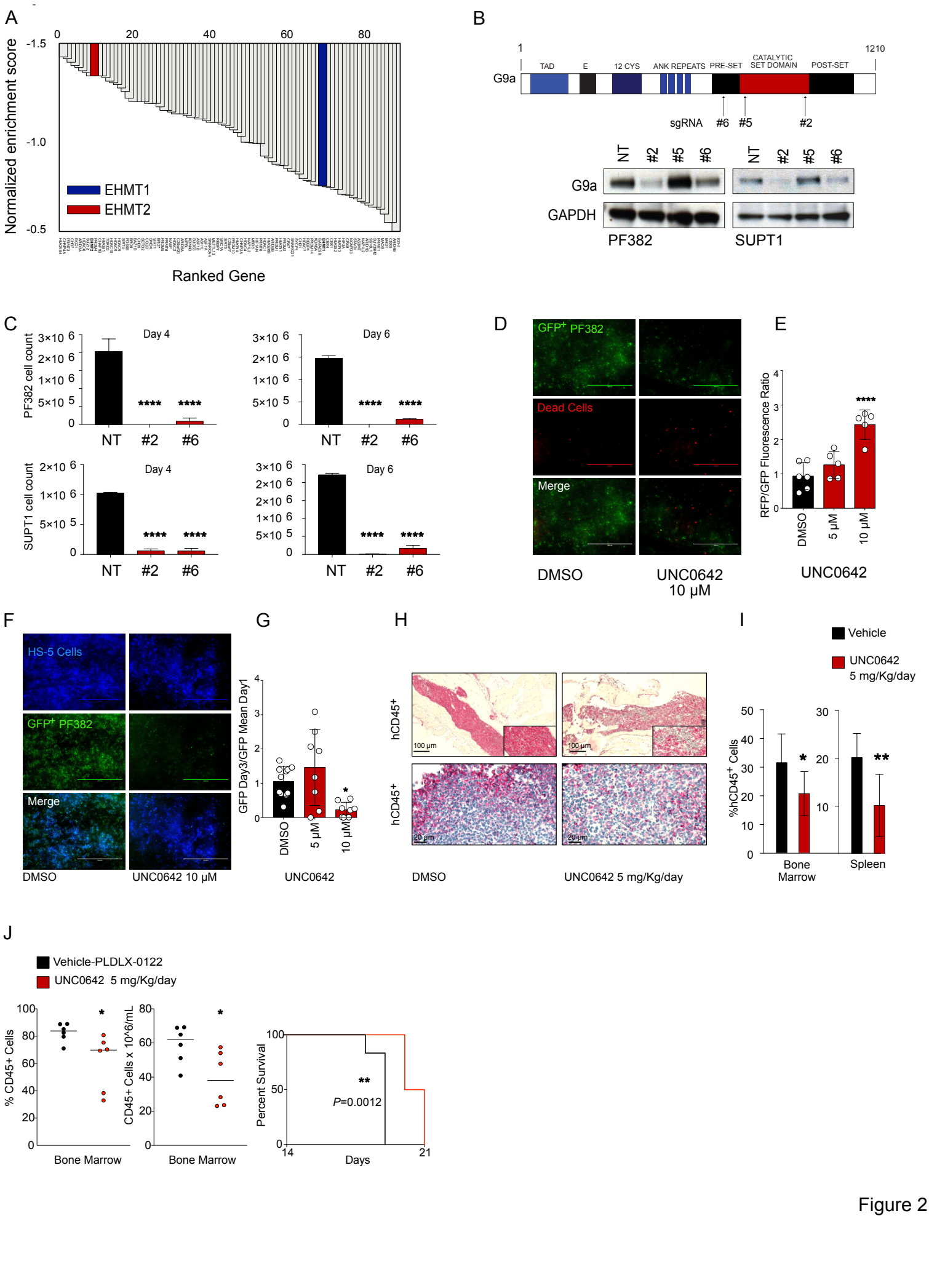
A
Normalized enrichment score
Ranked Gene
EHMT1
EHMT2
B
G9a
TAD
E
12 CYS
ANK REPEATS
PRE-SET
CATALYTIC SET DOMAIN
POST-SET
sgRNA #6 #5 #2
NT #2 #5 #6
GAPDH
PF382
SUPT1
C
PF382 cell count
SUPT1 cell count
Day 4
Day 6
D
GFP+ PF382
Dead Cells
Merge
DMSO
UNC0642 10 µM
E
RFP/GFP Fluorescence Ratio
UNC0642
F
HS-5 Cells
GFP+ PF382
Merge
DMSO
UNC0642 10 µM
G
GFP Day3/GFP Mean Day1
UNC0642
H
hCD45+
DMSO
UNC0642 5 mg/Kg/day
I
Vehicle
UNC0642 5 mg/Kg/day
%hCD45+ Cells
Bone Marrow
Spleen
J
Vehicle-PLDLX-0122
UNC0642 5 mg/Kg/day
% CD45+ Cells
CD45+ Cells x 10^6/mL
Bone Marrow
Percent Survival
P=0.0012
Days

Figure 2

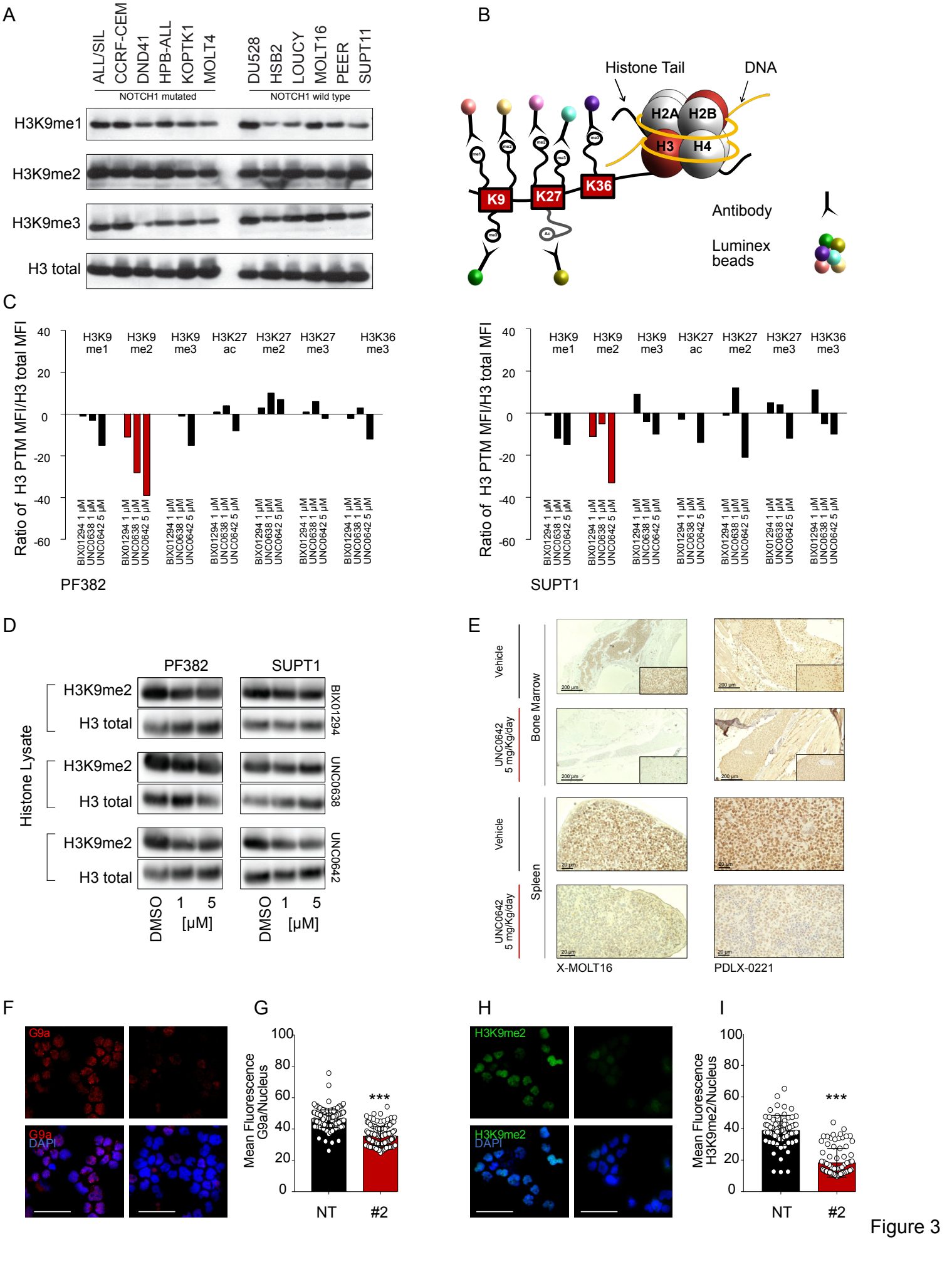
A
ALL/SIL
CCRF-CEM
DND41
HPB-ALL
KOPTK1
MOLT4
DU528
HSB2
LOUCY
MOLT16
PEER
SUPT11
NOTCH1 mutated
NOTCH1 wild type
H3K9me1
H3K9me2
H3K9me3
H3 total
B
Histone Tail
DNA
H2A
H2B
H3
H4
K9
K27
K36
Antibody
Luminex beads
C
Ratio of H3 PTM MFI/H3 total MFI
H3K9 me1
H3K9 me2
H3K9 me3
H3K27 ac
H3K27 me2
H3K27 me3
H3K36 me3
BIX01294 1 µM
UNC0638 1 µM
UNC0642 5 µM
PF382
SUPT1
D
PF382
SUPT1
Histone Lysate
H3K9me2
H3 total
BIX01294
UNC0638
UNC0642
DMSO
1
5
[µM]
E
Vehicle
UNC0642 5 mg/Kg/day
Bone Marrow
Spleen
X-MOLT16
PDLX-0221
F
G9a
DAPI
G
Mean Fluorescence G9a/Nucleus
***
NT
#2
H
H3K9me2
DAPI
I
Mean Fluorescence H3K9me2/Nucleus
***
NT
#2

Figure 3

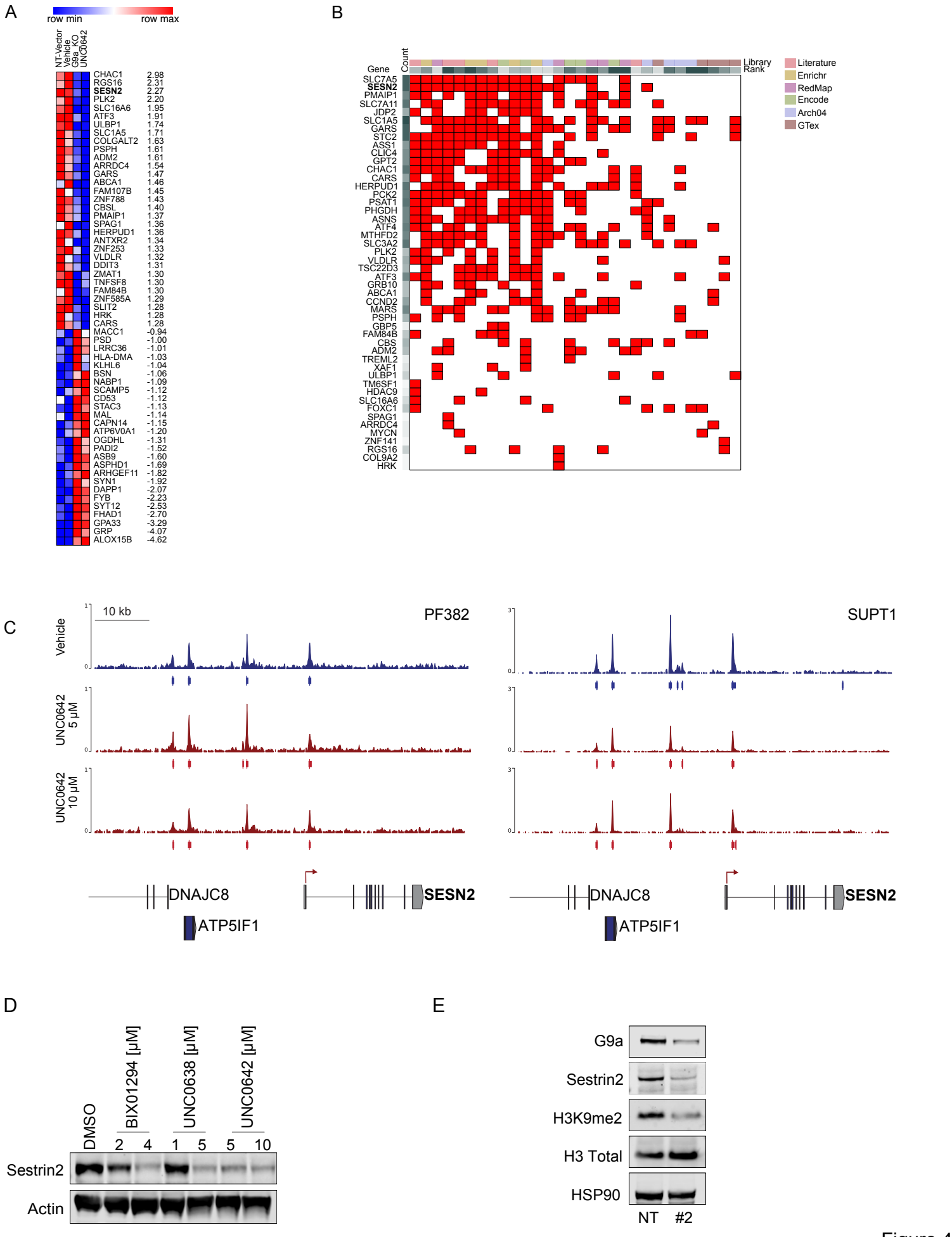
A
row min
row max
NT-Vector
Vehicle
G9a_KO
UNC0642
CHAC1 2.98
RGS16 2.31
SESN2 2.27
PLK2 2.20
SLC16A6 1.95
ATF3 1.91
ULBP1 1.74
SLC1A5 1.71
COLGALT2 1.63
PSPH 1.61
ADM2 1.61
ARRDC4 1.54
GARS 1.47
ABCA1 1.46
FAM107B 1.45
ZNF788 1.43
CBSL 1.40
PMAIP1 1.37
SPAG1 1.36
HERPUD1 1.36
ANTXR2 1.34
ZNF253 1.33
VLDLR 1.32
DDIT3 1.31
ZMAT1 1.30
TNFSF8 1.30
FAM84B 1.30
ZNF585A 1.29
SLIT2 1.28
HRK 1.28
CARS 1.28
MACC1 -0.94
PSD -1.00
LRRC36 -1.01
HLA-DMA -1.03
KLHL6 -1.04
BSN -1.06
NABP1 -1.09
SCAMP5 -1.12
CD53 -1.12
STAC3 -1.13
MAL -1.14
CAPN14 -1.15
ATP6V0A1 -1.20
OGDHL -1.31
PADI2 -1.52
ASB9 -1.60
ASPHD1 -1.69
ARHGEF11 -1.82
SYN1 -1.92
DAPP1 -2.07
FYB -2.23
SYT12 -2.53
FHAD1 -2.70
GPA33 -3.29
GRP -4.07
ALOX15B -4.62
B
Count
Gene
Library
Rank
Literature
Enrichr
RedMap
Encode
Arch04
GTex
SLC7A5
SESN2
PMAIP1
SLC7A11
JDP2
SLC1A5
GARS
STC2
ASS1
CLIC4
GPT2
CHAC1
CARS
HERPUD1
PCK2
PSAT1
PHGDH
ASNS
ATF4
MTHFD2
SLC3A2
PLK2
VLDLR
TSC22D3
ATF3
GRB10
ABCA1
CCND2
MARS
PSPH
GBP5
FAM84B
CBS
ADM2
TREML2
XAF1
ULBP1
TM6SF1
HDAC9
SLC16A6
FOXC1
SPAG1
ARRDC4
MYCN
ZNF141
RGS16
COL9A2
HRK
C
10 kb
PF382
SUPT1
Vehicle
UNC0642 5 µM
UNC0642 10 µM
DNAJC8
SESN2
ATP5IF1
D
DMSO
BIX01294 [µM]
UNC0638 [µM]
UNC0642 [µM]
2 4 1 5 5 10
Sestrin2
Actin
E
G9a
Sestrin2
H3K9me2
H3 Total
HSP90
NT #2

Figure 4

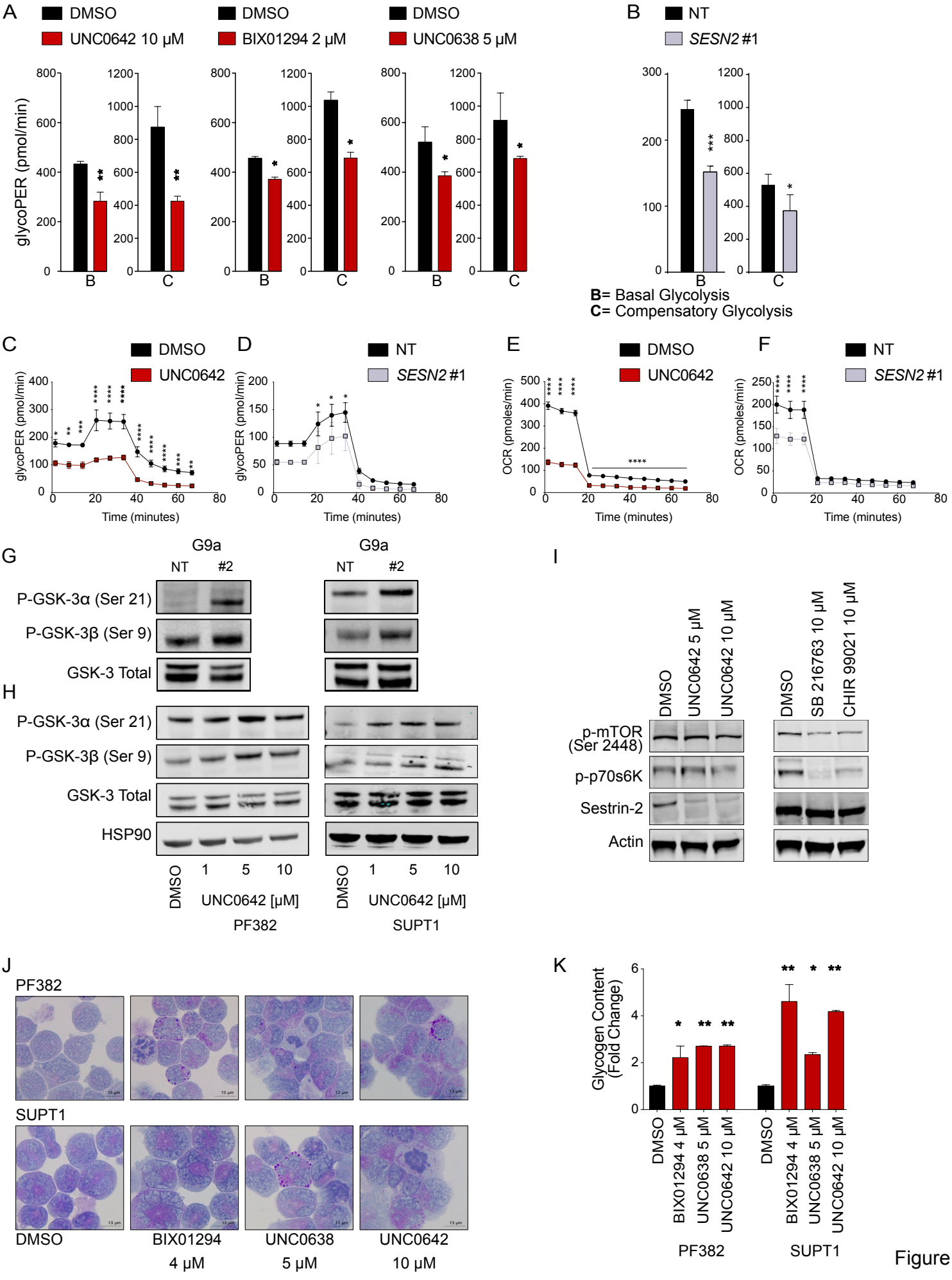
A
DMSO
UNC0642 10 µM
BIX01294 2 µM
UNC0638 5 µM
glycoPER (pmol/min)
B
C
B= Basal Glycolysis
C= Compensatory Glycolysis
B
NT
SESN2 #1
C
DMSO
UNC0642
D
NT
SESN2 #1
Time (minutes)
E
DMSO
UNC0642
OCR (pmoles/min)
F
NT
SESN2 #1
G
G9a
NT
#2
P-GSK-3α (Ser 21)
P-GSK-3β (Ser 9)
GSK-3 Total
H
HSP90
DMSO
1
5
10
UNC0642 [µM]
PF382
SUPT1
I
DMSO
UNC0642 5 µM
UNC0642 10 µM
SB 216763 10 µM
CHIR 99021 10 µM
p-mTOR (Ser 2448)
p-p70s6K
Sestrin-2
Actin
J
PF382
SUPT1
DMSO
BIX01294 4 µM
UNC0638 5 µM
UNC0642 10 µM
K
Glycogen Content (Fold Change)
BIX01294 4 µM
UNC0638 5 µM
UNC0642 10 µM
PF382
SUPT1

Figure 5

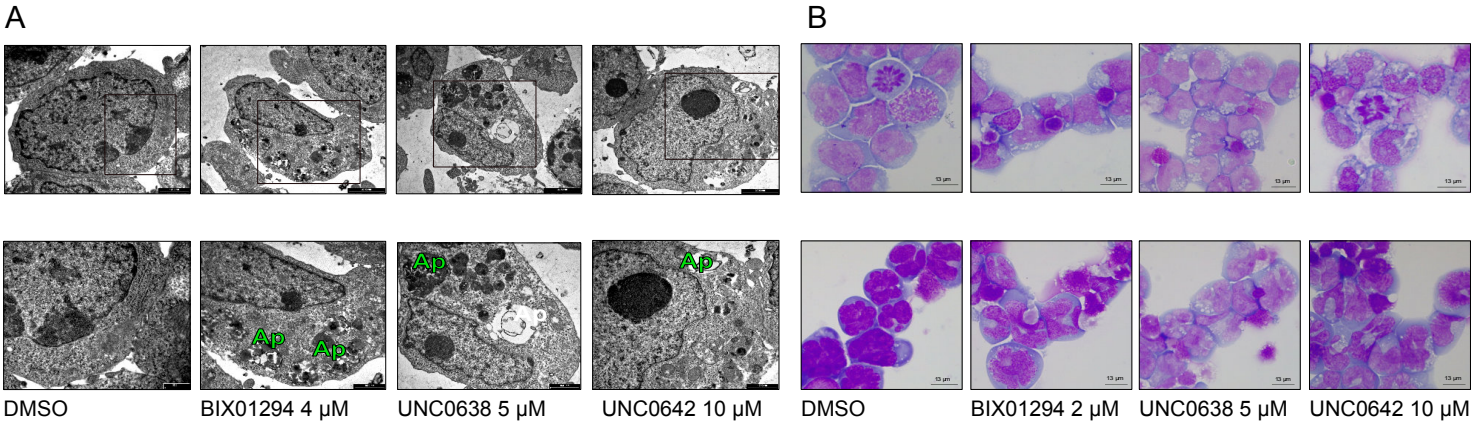
A
B
Ap
Ap
Ap
Ap
DMSO
BIX01294 4 μM
UNC0638 5 μM
UNC0642 10 μM
DMSO
BIX01294 2 μM
UNC0638 5 μM
UNC0642 10 μM

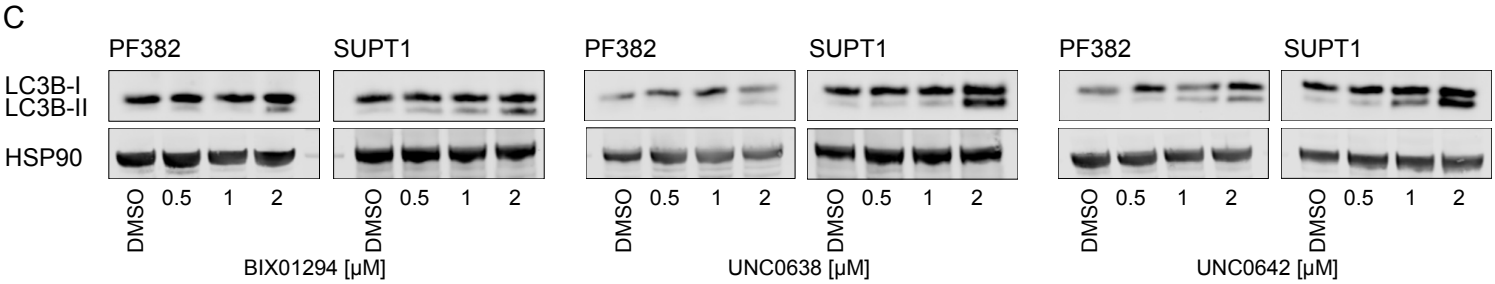
C
PF382
SUPT1
PF382
SUPT1
PF382
SUPT1
LC3B-I
LC3B-II
HSP90
DMSO 0.5 1 2 DMSO 0.5 1 2
BIX01294 [μM]
DMSO 0.5 1 2 DMSO 0.5 1 2
UNC0638 [μM]
DMSO 0.5 1 2 DMSO 0.5 1 2
UNC0642 [μM]

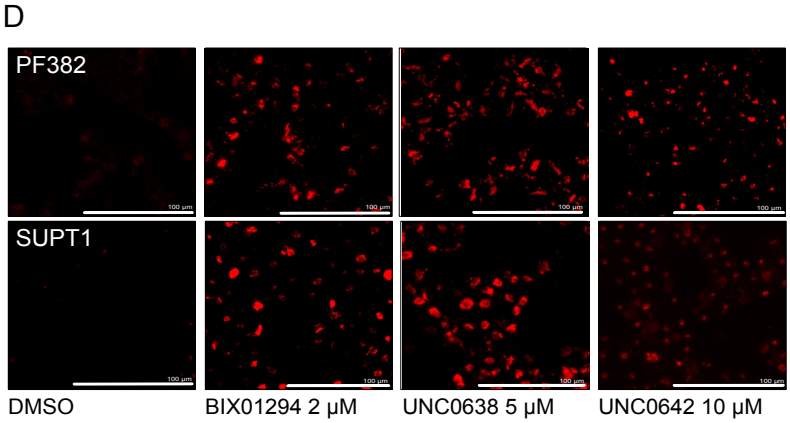
D
PF382
SUPT1
DMSO
BIX01294 2 μM
UNC0638 5 μM
UNC0642 10 μM

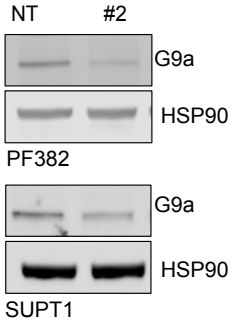
E
NT
#2
G9a
HSP90
PF382
G9a
HSP90
SUPT1

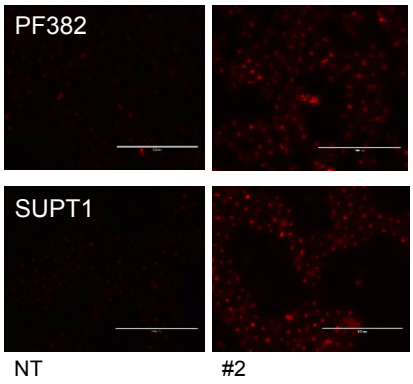
F
PF382
SUPT1
NT
#2

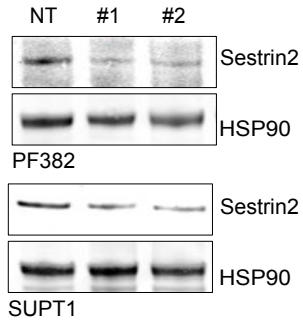
G
NT
#1
#2
Sestrin2
HSP90
PF382
Sestrin2
HSP90
SUPT1

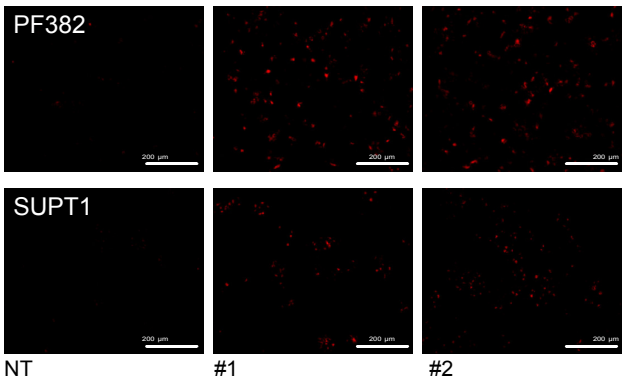
H
PF382
SUPT1
NT
#1
#2

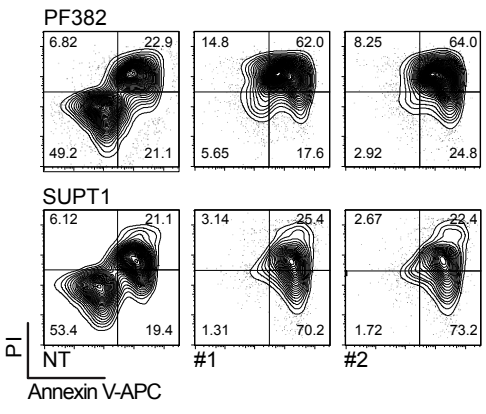
I
PF382
6.82
22.9
49.2
21.1
14.8
62.0
5.65
17.6
8.25
64.0
2.92
24.8
SUPT1
6.12
21.1
53.4
19.4
3.14
25.4
1.31
70.2
2.67
22.4
1.72
73.2
PI
NT
#1
#2
Annexin V-APC

Figure 6

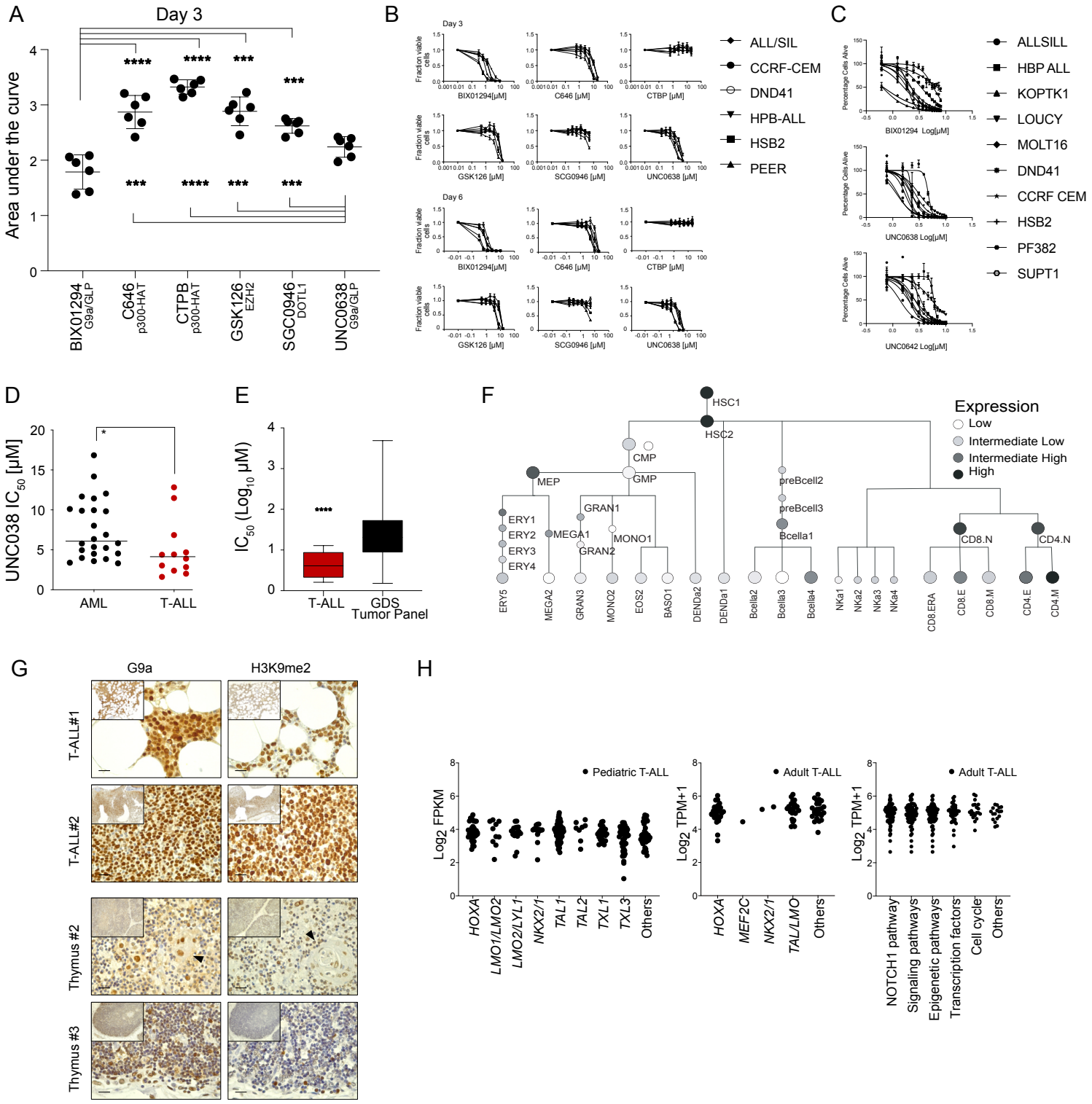

Supplementary Figure 1: (**A**) Effect of epigenetic modulators BIX01294, C646, CTPB, GSK126, SGC0946, and UNC0638 in T-ALL cell lines (ALL/SIL, CCRF-CEM, DND41, HPB-ALL, HSB2, and PEER) after three days of treatment. The scatter dot plot represents the effect of small molecules on cellular viability calculated using the area under the curve (AUC) model of log transformed dose-responses data using GraphPad V7. A lower AUC corresponds to a greater sensitivity. Effect of BIX01294, C646, CTPB, GSK126, SGC0946 and UNC0638) in T-ALL cell lines (listed) on cell viability after three (**B**) or six days of treatment. Error bars represent mean ± SD of three replicates. Graphs show fraction of viable cells relative to DMSO control as assessed by a CellTiter-Glo luminescence assay. (**C**) Effect of UNC0642 in T-ALL cell lines (listed) on cell viability after three days of treatment. Error bars represent mean ± SD of three replicates. Graphs show fraction of viable cells relative to DMSO control as assessed by a CellTiter-Glo luminescence assay.(**D**) Dotplot showing response (IC_{50}) to the G9a inhibitor UNC0638 in T-ALL or AML cell lines screened as part of the Genomics of Drug Sensitivity in Cancer Project (GDS) (**E**) Whisker plot showing response (IC_{50}) to the G9a inhibitor UNC0638 in over 600 cancer cell in GDS. T-ALL cell lines are indicated in red and all other cancer cell lines in black. The line in the box-and-whisker diagram represents the IC_{50} median. The upper edge (hinge) of the box indicates the 75th percentile of the data set, and the lower hinge the 25th percentile. The ends of the vertical line indicate the minimum and the maximum data values. Statistical significance among groups (****$P < 0.0001$) was determined by a non-parametric t-test (Mann-Whitney). (**F**) Expression of *EHMT2* in the hematopoietic Differentiation Map (DMAP) database [37]. A gray scale is applied for increased expression. Black circles on the lineage tree represent high *EHMT2* expression on a spectrum, while the pale grey circles show lower *EHMT2* expression.(**G**) G9a and H3K9me2 expression in formalin-fixed paraffin embedded thymus and bone marrow leukemia samples. Scale bar 20 µm. arrowheads point to Hassal's corpuscles (**H**) *EHMT2* expression with respect to recurring genetic alteration in pediatric (PMID 28671688) and adult (PMID 29279377) T-ALL clinical samples.

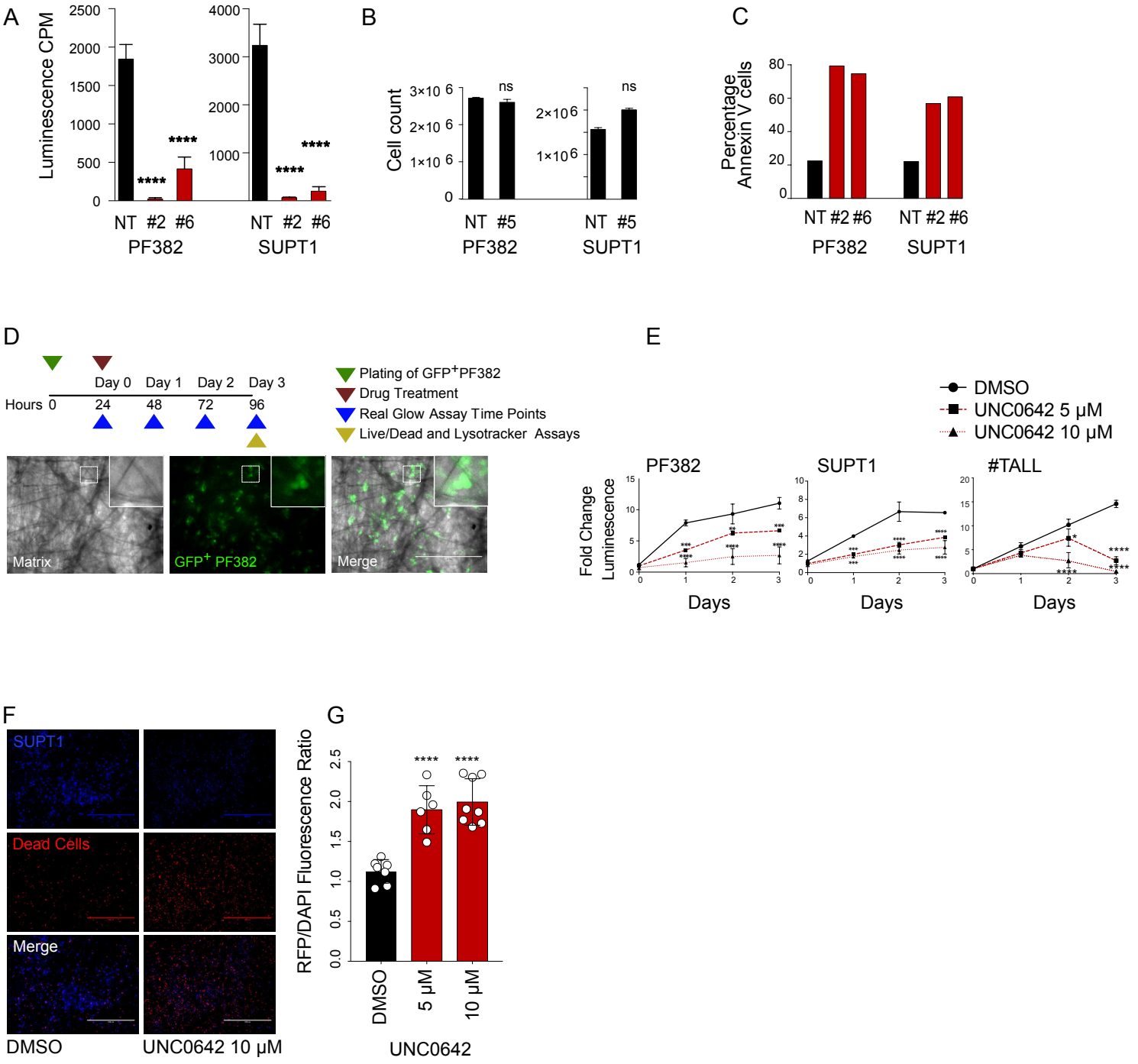

Supplementary Figure 2: (**A**) Effect of G9a knockout in PF382 or SUPT1 cells at six days post sgRNA selection. Histograms show ATP/luminescence count per minute (CPM). Error bars denote the mean ± standard deviation (SD) of a minimum of three biological replicates. Statistical significance among groups (****P < 0.0001) was determined by a non-parametric t-test (Mann-Whitney).NT=non-targeting, #2 =sgRNA number 2, #6 =sgRNA number 6 (**B**) Effect of sgRNA #5 guide in PF382 and SUPT1 cells. Histograms show trypan exclusion assay absolute cellular count. Error bar denotes the mean ± standard deviation (SD) of a minimum of three biological replicates. Statistical significance among groups (P=0.2 PF382, P=0.1 SUPT1 not significant) was determined by non-parametric t-test (Mann-Whitney). NT=non-targeting, #2 =sgRNA number 2. (**C**) Effect of G9a loss in PF382 and SUPT1 cells on induction of apoptosis. Annexin V/PI staining of PF382 and SUPT1 cells six days post sgRNA selection. Histograms show percentage of annexin V positive cells. NT=non-targeting, #2 =sgRNA number 2, #6 =sgRNA number 6. (**D**) Outline of the experiment (top of the panel). Representative picture of growing GFP positive (GFP+) PF382 cells on the inner polyester matrix of VITVO 3D bioreactor (bottom panel). (**E**) Cell viability assay of PF382 , SUPT1, and primary T-ALL cells in 3D culture treated with DMSO or UNC0642 at the indicated concentrations. T-ALL proliferation was assessed at the indicated time points using Real Time-GLO™ MT Assay and plotted as the luminescence (of the total colonized matrix) fold increase relative to Day 0. Error bars denote the mean ± standard deviation (SD) of three biological replicates. (**F**) Live Dead assay of SUPT1 (blue) cells growing in 3D cell culture treated with DMSO or UNC0642 at the indicated concentrations. Representative immunofluorescence images of control or UNC0642 treated SUPT1 upon a fluorescent based Live/Dead® assay staining at 72 hours. Cell death is indicated in the histogram (**G**) as a fluorescence ratio between DAPI (viable cells) and RFP (dead cells) signals of the acquired fields. Error bars denote the mean ± standard deviation (SD) of one representative experiment. For imaging quantification, we selected fields with minor autofluorescence of the scaffold's matrix and no air bubbles. Images were captured by an EVOS FL microscope using Olympus long distance 4x objective (scale bar 1000 μm). Statistical significance among groups (*$P \leq 0.05$, **$P \leq 0.01$, ***$P \leq 0.001$, ****$P < 0.0001$) for all the experiments was determined by one-or two-way ANOVA (using Bonferroni's correction for multiple comparison testing).

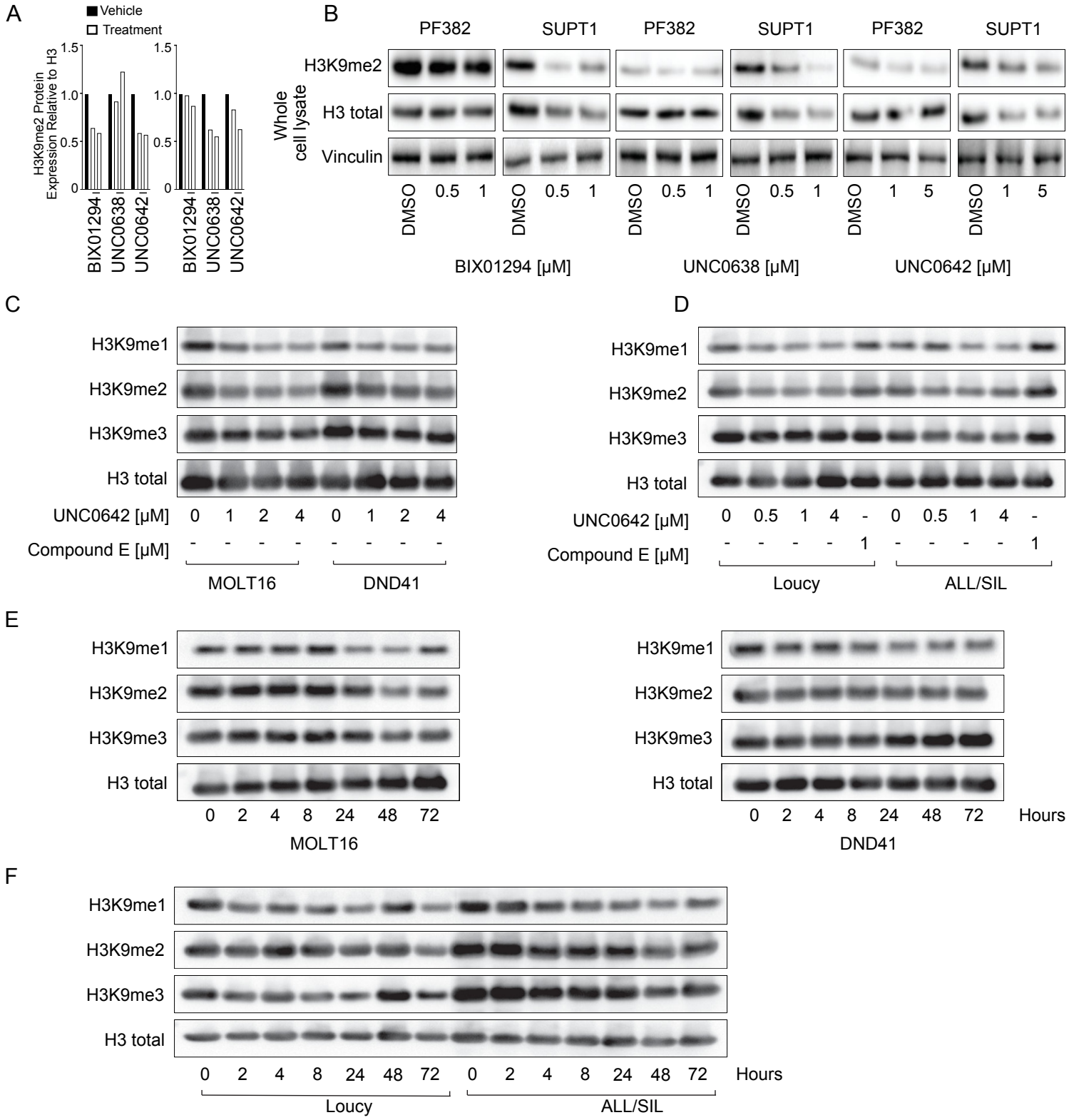

Supplementary Figure 3: (**A**) H3K9me2 expression relative to H3 from histone extracted G9a inbibitors treated cells(**B**) Western immunoblotting showing expression of H3K9me2 in PF382 and SUPT1 cells treated at the indicated concentrations of G9a inhibitors for 48 hours. Protein lysates were obtained using a whole cells extraction protocol and stained with an antibody recognizing the H3K9me2 residue or total H3 with vinculin used as a loading control. (**C**) Western immunoblotting showing expression of H3K9me1, H3K9me2, and H3K9me3 in MOLT16 and DND41 cells treated at the indicated concentrations of UNC0642 for 48 hours. Protein lysates were obtained using an acidic histone extraction protocol, stained with an antibody recognizing the H3K9me1-3 residues. Total H3 was used as a loading control. (**D**) Western immunoblotting showing expression of H3K9me1, H3K9me2, and H3K9me3 in Loucy and ALL/SIL cells treated at the indicated concentrations of UNC0642 or Compound E for 48 hours. Protein lysates were obtained using acidic histone extraction protocol and stained with an antibody recognizing the H3K9me1-3 residues. Total H3 was used as a loading control. (**E**) Western immunoblotting showing time course dependent expression of H3K9me1, H3K9me2, and H3K9me3 in MOLT16 and DND41 cells treated with UNC0642 1 μM. Protein lysates were obtained using an acidic histone extraction protocol and stained with an antibody recognizing the H3K9me1-3 residues. Total H3 was used as a loading control. (**F**) Western immunoblotting showing time course dependent expression of H3K9me1, H3K9me2, and H3K9me3 in Loucy and ALL/SIL cells treated with UNC0642 1 μM. Protein lysates were obtained using an acidic histone extraction protocol and stained with an antibody recognizing the H3K9me1-3 residues. Total H3 was used as a loading control.

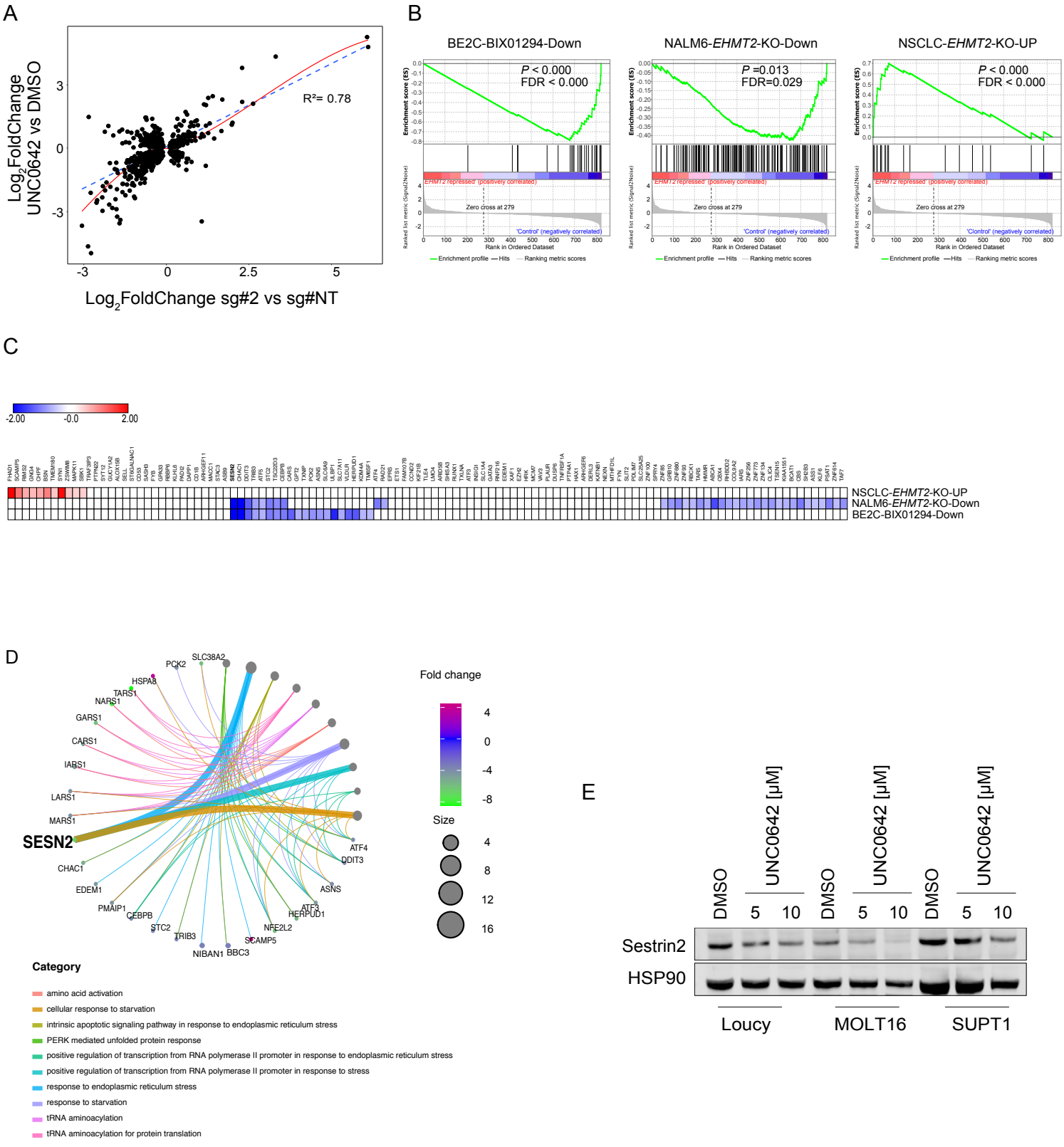

Supplementary Figure 4: (**A**) Dot plot showing significant gene expression changes in sg#2 versus sgNT or treated either with vehicle or UNC0642 ($P < 0.05$ and Log_2 fold changes >1.5) in PF382 cells. Pearson linear regression model is shown. (**B**) GSEA plot showing the enrichment of the genes down regulated by *EHMT2* in the two representative G9a "off" gene sets (BIX01294 top panel; *EHMT2* CRSPR-Cas9 knockout bottom panel). (**C**) Leading edge analysis of enriched genes. In the grid, the rows represent genes that constitute the main enrichment, leading edge (blue for down-regulated genes, red for up regulated genes), in the different genes sets (column). (**D**) Circular net plot showing the network of differentially expressed genes in the first ten most strongly associated Gene Ontology (GO) processes. The size of each gray nodes represents the number of overlapped genes in each term and the colored scale bar represents the Log_2 fold change of each differentially expressed gene. (**E**) Western immunoblotting showing expression of sestrin-2 in PF382 and SUPT1 cells 48 hours post G9a inhibitors treatment. Protein lysates were stained with an anti-sestrin-2 antibody. HSP90 was used as loading control.

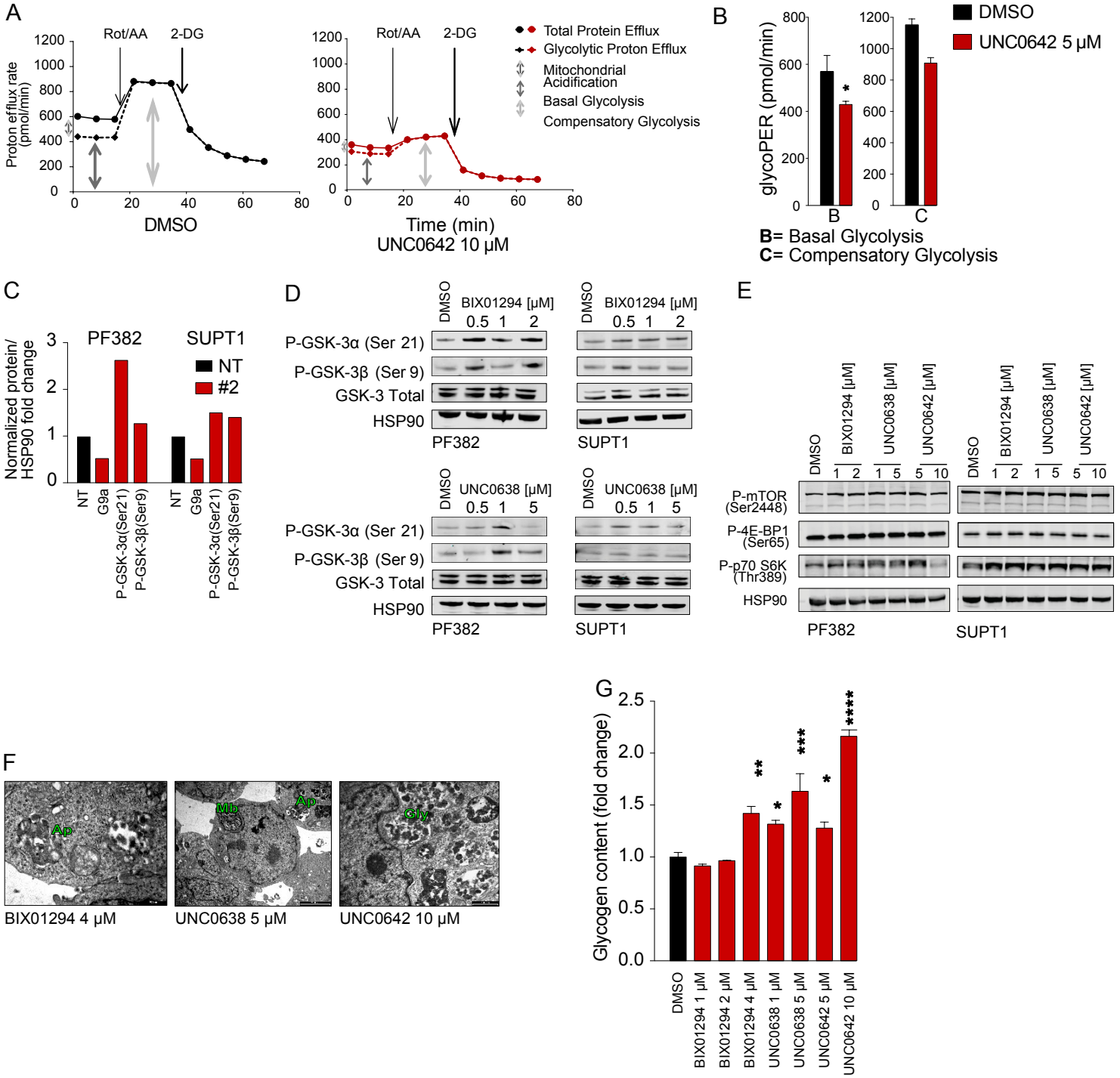

Supplementary Figure 5: (**A**) Representative Glycolytic Rate Assay profiled in PF382 cells treated with either DMSO or UNC0642. Proton efflux from live cells comprises both glycolytic and mitochondrial derived acidification. Inhibition of mitochondrial function by injecting rotenone & antimycin A (Rot/AA) enables calculation of mitochondrial-associated acidification. Subtraction of mitochondrial acidification from Total Proton Efflux Rate (PER) results in Glycolytic Proton Efflux Rate. The second injection is 2-deoxy-D-glucose (2-DG), which inhibits glycolysis. The resulting decrease in proton efflux rate provides qualitative confirmation that the PER produced prior to the injection is primarily due to glycolysis. (**B**) Glycolytic phenotype in PF382 cells. Histograms represent mean ± SD of three replicates of PF382 T-ALL cells treated with DMSO and UNC0642 (5 μM) on the x-axis. The y-axis represents the glycolytic proton efflux rate (PER) at the basal and compensatory level. Statistical significance among groups (*$P < 0.05$) was determined by a non-parametric t-test (Mann-Whitney). (**C**) Densitometric quantification of indicated proteins after two days days post sgRNA selection in PF382 and SUPT1 cells. The relative intensity of G9a/EHMT2, P-GSK-3α (Ser21) and P-GSK-3β (Ser9) was normalized for the levels of HSP90 and expressed as fold change relative to non-targeting (NT) sgRNA guide. (**D**) Modulation of GSK-3 by the G9a inhibitor BIX01294 and UNC0638. Western immunoblot showing phosphorylation of serine-9 in GSK-3β or serine-21 in GSK-3α in T-ALL. Cell lysates were obtained after 48 hours treatment. Protein lysates were stained with P-GSK-3α (Ser21), P-GSK-3β (Ser9), or GSK-3 Total. HSP90 was used as a loading control. (**E**) Western immunoblot showing phosphorylation of Ser2448 in mTOR, Ser65 in 4E-BP1, Thr389 in p70 S6K. Lysates were obtained after 24 hours treatment, HSP90 was used as a loading control. (**F**) Transmission Electron Microscopic (TEM) images of T-ALL cells exposed for 48 hours to G9a inhibitors. Autophagosomes (Ap) displaying multilamellar bodies (Mb) or compartmentalization of electron dense material corresponding to glycogen granules (gly). Scale Bars: left 0.5 μm; center 2 μm; right 1 μm. For DMSO see micrographs in Figure 6A and Supplementary Figure 6B. (**G**) Effect of G9a inhibitors BIX01294, UNC0638, and UNC0642 on cellular glycogen content. Histograms show the glycogen fold change increase relative to a DMSO control after G9a inhibitor treatment for 48 hours in the SUPT1 cell line. Error bars denote the mean ± standard deviation (SD) of two biological replicates. Statistical significance among groups (***$P < 0.001$, ****$P < 0.0001$) was determined by a non-parametric t-test (Mann-Whitney).

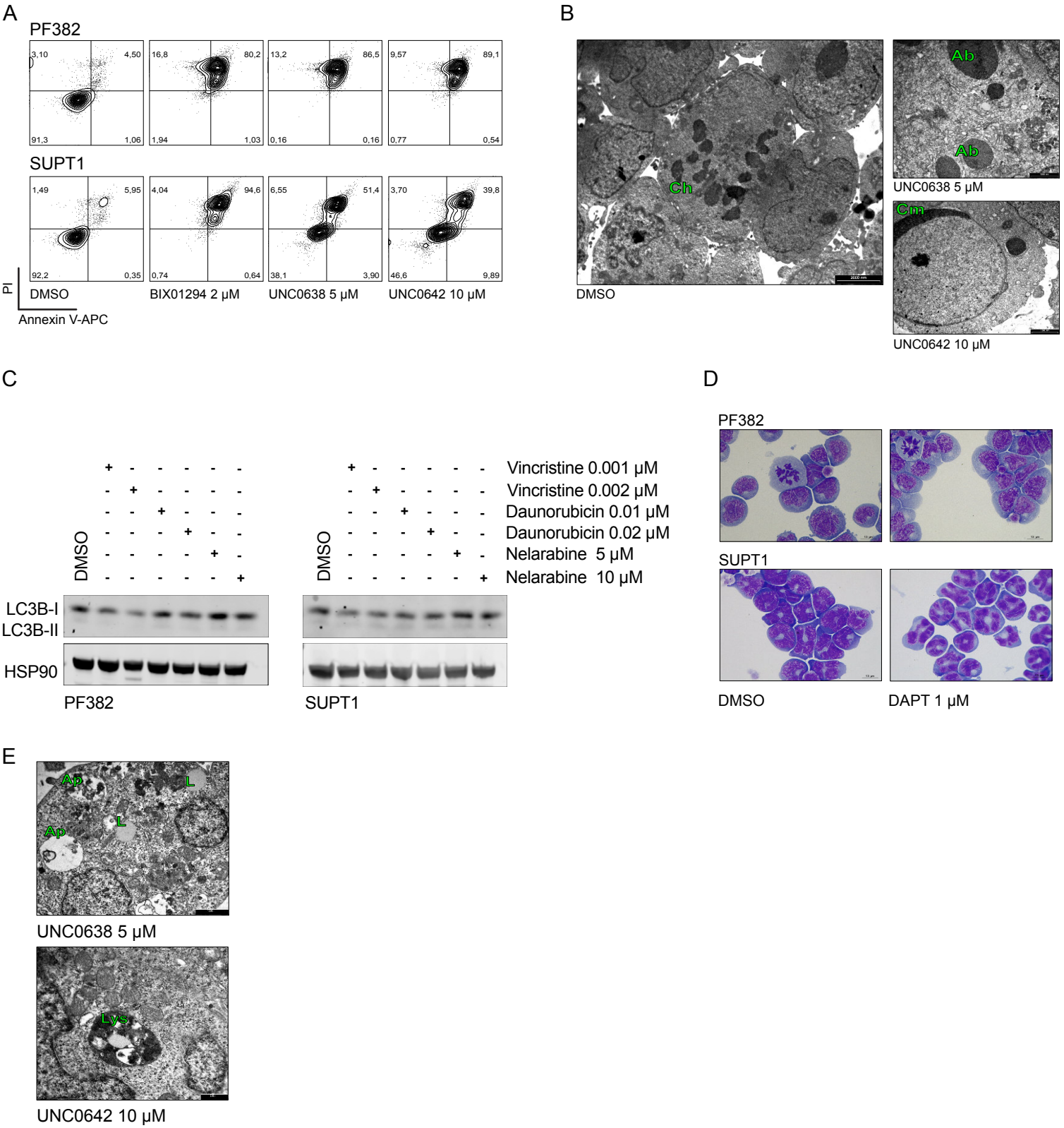

Supplementary Figure 6: (**A**) Effect of G9a inhibitors treatments on induction of apoptosis. Annexin V/PI staining of T-ALL cells following 48 hours of treatment with the indicated concentrations of BIX01294, UNC0638, and UNC0642. A minimum of 20,000 events was collected for each condition. (**B**) Transmission Electron Microscopic (TEM) image of untreated (DMSO) T-ALL cells one of which shows mitotic chromosomes (Ch). Scale bar: 2 µm. The two right panels illustrate cultures of the PF382 cell line exposed for 48 hours to the indicated concentrations of different G9a inhibitors. Apoptotic features are documented by round cytoplasmic apoptotic bodies (Ab, upper) and a nucleus undergoing DNA degradation and chromatin margination (Cm, lower). Scale bars: 1 µm. (**C**) Western immunoblotting showing expression of LC3B-I and LC3B-II in PF382 and SUPT1 cells treated at with vincristine, daunorubicine or nelarabine at the indicated concentrations after 48 hours. HSP90 was used as a loading control. (**D**) Representative images of May Grunwald-Giemsa stained cytospin preparations of T-ALL (PF382 and SUPT1) cultured in vehicle (DMSO) or DAPT for 48 hours. Images were captured with a Leica ICC50W optical microscope (100X). Scale bars: 13 µm. (**E**) High magnification TEM images of G9a inhibitor-treated T-ALL cells to illustrate the ultrastructural characteristics of autophagosomes (Ap) and the presence of free lipid droplets (L) or engulfed by phagolysosomes (Lys). Scale Bars: top 1 µm; bottom 0.5 µm.

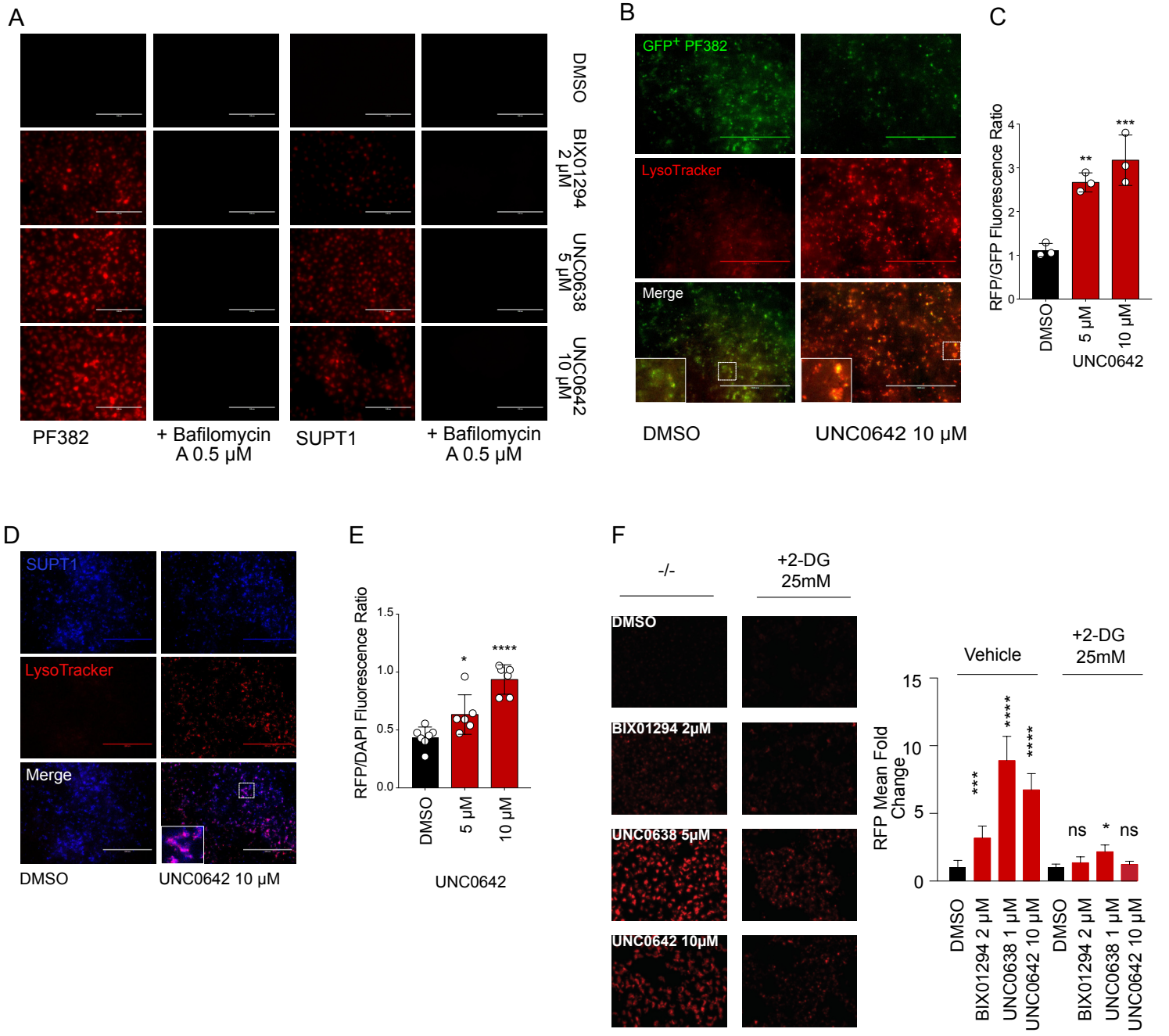

Supplementary Figure 7: (**A**) LysoTracker® Red DND-99 staining of T-ALL cells treated at the indicated concentrations of G9a inhibitors and 0.5 μM Bafilomycin A for 48 hours. Scale bars: 100 μm. (**B**) Induction of autophagy in UNC0642 treated PF382 growing in 3D bioreactors. Autophagosome/lysosome formation was evaluated by the fluorescence based LysoTracker assay. Images were captured by EVOS FL microscope using Olympus long distance 4x objective. Scale bar: 1000 μm. (**C**) Induction of autophagy in UNC0642 treated PF382 growing in 3D cell culture bioreactor. Autophagosome/lysosome formation was evaluated by the fluorescence based and quantified as fluorescence ratio between RFP (acidic vesicles) and GFP (viable cells) signals of the acquired fields (on the bottom). Error bars denote the mean ± standard deviation (SD) of one representative experiment. For imaging quantification, we selected fields with minor autofluorescence of the scaffold's matrix and no air bubbles. (**D**) Induction of autophagy in UNC0642 treated SUPT1 cells growing in a 3D cell culture bioreactor. Autophagosome/lysosome formation was evaluated by the fluorescence based LysoTracker assay and quantified (**E**) as fluorescence ratio between RFP (acidic vesicles) and blue (viable cells) signal per acquired fields. Error bars denote the mean ± standard deviation (SD) of one representative experiment. For imaging quantification, we selected fields with minor autofluorescence of the scaffold's matrix and no air bubbles. Images were captured by an EVOS FL microscope using Olympus long distance 4x objective (scale bar 1000 μm). Statistical significance among groups (*$P \leq 0.05$, **$P \leq 0.01$, ***$P \leq 0.001$, ****$P < 0.0001$) for all the experiments was determined by one-or two-way ANOVA (using Bonferroni's correction for multiple comparison testing). (**F**) LysoTracker® Red DND-99 labeled T-ALL cells treated with G9a inhibitors in the presence or absence of 25 mM 2-Deoxy- d-glucose (2-DG). Scale Bars: 100 μm. Histograms show the mean and standard deviation of RFP per field (n=9) relative to the vehicle control. Statistical significance among groups (*$P < 0.05$, ***$P < 0.001$, ****$P < 0.0001$) was determined by a non-parametric t-test (Mann-Whitney)